OTDOA-Based Positioning in NB-IoT

Axel Berg
tfy13ab1@student.lth.se

Department of Electrical and Information Technology
Lund University

Supervisor: Fredrik Tufvesson (EIT),
Sha Hu (EIT),
Michal Stala (ARM)

Examiner: Fredrik Rusek (EIT)

June 19, 2017

Printed in Sweden
Tryckeriet i E-huset, Lund

Abstract

This thesis considers the problem of improving the performance of observed time difference of arrival (OTDOA) based positioning for Narrowband Internet of Things (NB-IoT). A new iterative low-complexity algorithm based on expectation maximization successive interference cancellation (EM-SIC) is presented. The algorithm tackles the near-far problem by using an iterative SIC, where for each received signal a frequency offset compensation and channel estimation is performed. A low receiver sampling rate of 1.92 MHz is assumed and the time of arrival (TOA) estimates are refined by interpolation of correlation results to a higher sampling rate. At the final stage of the algorithm, the problem of multipath fading is addressed using an iterative first-path detector. It is shown that the proposes EM-SIC algorithm greatly increases positioning performance compared to conventional methods and the estimated TOA variance almost attains the Cramér-Rao lower bound.

The works of the LORD are great,
sought out of all them that have pleasure therein
- Psalm 111:2

Popular Science Summary

The internet of things (IoT) is the infrastructure that enables the connectivity of smart devices to the internet. It has been estimated that around 100 billion devices will be connected by 2025 and this fast growth is expected to revolutionize many industries, such as healthcare, transportation, and agriculture. As of today, many everyday items are already being connected in smart home applications. Due to the wide range of applications, there are many different emerging standards for enabling the IoT. Narrowband IoT (NB-IoT) is a cellular technology that will allow connectivity for devices in remote areas while allowing for very long battery lifetimes, which is critical in some applications.

In the next release of NB-IoT, a new feature has been added that will allow positioning of devices by allowing them to receive signals from several cell towers simultaneously. Examples of applications of this feature are fleet management, network capacity planning, and navigation services. The used positioning technique is known as observed time difference of arrival (OTDOA), because the device measures the arrival time of several transmitted reference signals. By using the difference between the observed arrival times, the position of the device can be estimated. However, this technique has several limitations which makes it difficult to obtain good position accuracy. Since NB-IoT is technique that focuses on low-end devices, there has been a trade off where system capacity has been sacrificed in order to achieve low complexity. Therefore it is especially challenging to implement OTDOA-based positioning in NB-IoT. For example, the bandwidth of the reference signals is very small, which makes it difficult to locate them in time. Furthermore, the large distances covered by NB-IoT cell towers causes the received signal powers to be very weak. Smart techniques are therefore necessary in order to correctly locate an NB-IoT device.

In this thesis, a low-complexity OTDOA-based positioning algorithm that strives to overcome the challenges of NB-IoT networks has been implemented. The algorithm improves the positioning accuracy by cancelling interfering signals from neighbouring cell towers, estimating the frequency offset of each received signal and converting the results to a higher sampling frequency. Such methods have been used on their own in other cellular technologies, whereas in the algorithm proposed in this thesis, they are combined and applied to the specific scenario of positioning for NB-IoT. It is shown that the new algorithm increases positioning performance significantly compared to conventional methods. In particular, the

probability that a given user equipment can be localized is greatly increased, as well as the accuracy of the estimated position. Furthermore, an analysis of the computational complexity of the algorithm shows that it can be realistically implemented in user equipment hardware and software. However, the performance increases are not as great in urban environments where signals can scatter on buildings and other large objects, and this is an area of development for future work.

Acknowledgements

I would like to thank ARM Sweden for giving me the opportunity to write my thesis on this topic. A special thanks to Michal Stala for supervising me and giving me feedback on my work. Furthermore, I would like to express my gratitude to Sha Hu for helping me develop the contents and ideas of this thesis. Without his help, the findings of this thesis would not have been possible. Finally, I give thanks to my fiancée Anna for her love and encouragement throughout my work.

Axel Berg

List of Acronyms

3GPP 3rd Generation Partnership Project

A-GNSS Assisted Global Navigation Satellite System

AOA Angle of Arrival

AWGN Additive White Gaussian Noise

BS Base Station

CDF Cumulative Distribution Function

CE Channel Estimation

CFO Carrier Frequency Offset

CP Cyclic Prefix

CRLB Cramér-Rao Lower Bound

DFT Discrete Fourier Transform

E-CID Enhanced Cell-ID

EM Expectation Maximization

eNodeB evolved Node B

ETU Extended Typical Urban

FFT Fast Fourier Transform

FOC Frequency Offset Compensation

IoT Internet of Things

LAN Local Area Network

LMMSE Linear Minimum Mean Square Error

LOS Line of Sight

LPWAN Low Power Wide Area Network

LS Least Squares

LTE Long Term Evolution

M2M Machine to Machine

ML Maximum Likelihood

MPD Multi Path Detection

NB-IoT Narrowband Internet of Things

NFC Near Field Communications

NPRS Narrowband Positioning Reference Signal

OFDM Orthogonal Frequency Division Multiplexing

OTDOA Observed Time Difference of Arrival

PAN Personal Area Network

PAR Peak To Average

PDF Probability Distribution Function

PRB Physical Resource Bloc

QPSK Quadrature Phase Shift Keying

RB Resource Block

RE Resource Element

RSS Received Signal Strength

SIC Successive Interference Cancellation

SINR Signal to Noise and Interference Ratio

SNR Signal to Noise Ratio

TDOA Time Difference of Arrival

TOA Time of Arrival

UE User Equipment

WAN Wide Area Network

Table of Contents

List of Figures

List of Tables

Chapter 1
Introduction

This thesis investigates the challenges of implementing observed time difference of arrival (OTDOA) based positioning for Narrowband Internet of Things (NB-IoT), which will be integrated as a part of the 3rd Generation Partnership Project (3GPP) Long Term Evolution (LTE) release 14. ARM Cordio-N IP for NB-IoT will provide the wide area and low power connectivity required for low-end IoT devices. It consists of RF and baseband hardware, together with software layers 1, 2 and 3 [1]. This thesis has been carried out in order to develop a novel low-complexity algorithm for time of arrival estimation that will be implemented in layer 1 hardware and software. The algorithm is evaluated under different radio environments and its positioning performance is compared to standard techniques.

The outline of this thesis is as follows:

Chapter 2 gives an introduction to the subject and presents relevant background information

Chapter 3 explains the specifics of OTDOA-based positioning for NB-IoT according to 3GPP standardizations and covers some of the associated challenges, as well as related previous work

Chapter 4 presents the novel algorithm along with a brief analysis of its computational complexity

Chapter 5 presents results from numerical simulations where the performance of the new algorithm is evaluated

Chapter 6 draws the conclusions from the simulation results and outlines future work

Chapter 2
Background

2.1 The Internet of Things

The Internet of Things (IoT) is a loosely defined term referring to the network of smart object, sensors and everyday items that can gather and exchange data with each other and with the cloud. Some applications of the IoT are smart homes, smart cities, smart grids, healthcare, automotive, manufacturing, logistics and supply chain management [2]. It has been estimated that around 100 billion IoT devices, corresponding to an economic impact of $11 trillion, will be connected by 2025 [3].

There are several available and emerging communication standards for enabling the IoT. Depending on the application, they can be based on either near field communications (NFC), personal area networks (PAN), such as Bluetooth and ZigBee, local area networks (LAN), for example Wi-Fi, or wide area networks (WAN). The last category consists of both unlicensed low powered WAN (LPWAN), such as LoRa and SigFox, and cellular technologies. Among cellular technologies that operate on licenced spectrum are GSM, WCDMA, LTE and upcoming 5G standards. However, these have primarily been developed for voice and high-throughput data services, which make them unfit for many IoT applications that do not require high data throughput, but other aspects such as low device costs, long battery life, deep indoor coverage and large capacity can be critical [4].

2.2 NB-IoT

NB-IoT is an emerging cellular standard for machine-to-machine (M2M) type communications that was introduced in 3GPP Release 13 [5, 6]. The purpose of the new standard is to provide wide-area coverage for massive IoT deployments. NB-IoT is based on existing LTE specifications and can therefore co-exist with current LTE networks. Many aspects of LTE have been reused, such as the modulation scheme, multiple access methods, channel coding, rate matching etc. NB-IoT is designed for 180 kHz system bandwidth, which makes it possible to deploy NB-IoT inside an existing LTE carrier by replacing one of its physical resource blocks (PRB), a so called in-band deployment scenario. It can also be deployed in the guard-band of an LTE carrier, or in so called standalone mode, by replacing an existing GSM carrier.

Some of the performance objectives for NB-IoT are:

- **Low device costs:** support for ultra-low-complexity devices, using only one receive antenna operating at a low sampling rate.
- **Low data rates:** 250 kb/s physical layer peak data rate [7], which is suitable for ultra-low-end devices.
- **Extended coverage:** 20 dB higher maximum coupling loss compared to LTE [8], which allows for very large cell sizes and improved indoor coverage.
- **Increased capacity:** at least 52 500 user equipments (UEs) per sector will be supported [9].
- **Increased battery lifetime:** up to 10 years of UE battery lifetime, assuming that an average of 200 bytes of data is being transmitted per day [9].

These qualities give NB-IoT an advantage over current cellular technologies in enabling massive deployments of low-end IoT devices. The specification for NB-IoT in 3GPP Release 13 was frozen in June 2016 [6] and the positioning features available in LTE were not carried over to NB-IoT. However, this feature, along with several other enhancements, is going to be introduced as a part of the new specification in 3GPP Release 14 [10]. The positioning procedure is described in more detail in Chapter 2.

2.3 OFDM

Orthogonal Frequency Division Multiplexing (OFDM) is a method of transmitting digital symbols over several parallel data streams [11, 12]. The symbols are modulated with an arbitrary modulation scheme and transmitted over orthogonal subcarriers. Consider a set of complex symbols $X[k]$, where $k = 0, ..., N_{sc} - 1$ denotes the subcarrier index. The baseband OFDM signal can then be represented as

$$x(t) = \sum_{k=0}^{N_{sc}-1} X[k] e^{j2\pi\Delta f k t}, \quad 0 \leq t < T_u \tag{2.1}$$

where Δf is the subcarrier spacing and $T_u = 1/\Delta f$ is the symbol duration. Under ideal conditions, this choice of symbol duration guarantees subcarrier orthogonality, since

$$\int_0^{T_u} e^{j2\pi\Delta f k_1 t} \left(e^{j2\pi\Delta f k_2 t} \right)^* = 0, \quad \text{for } k_1 \neq k_2 \tag{2.2}$$

for this particular choice of T_u. However, in time-dispersive fading channels, the orthogonality between subcarriers will be lost unless a guard interval is inserted between the OFDM symbols. Therefore, a cyclic prefix (CP) is implemented by copying the last portion of each symbol with duration T_{CP} and inserting it prior to the symbol start, such that

$$x(t) = x(t + T_u + T_{CP}), \quad -T_{CP} \leq t < 0 \tag{2.3}$$

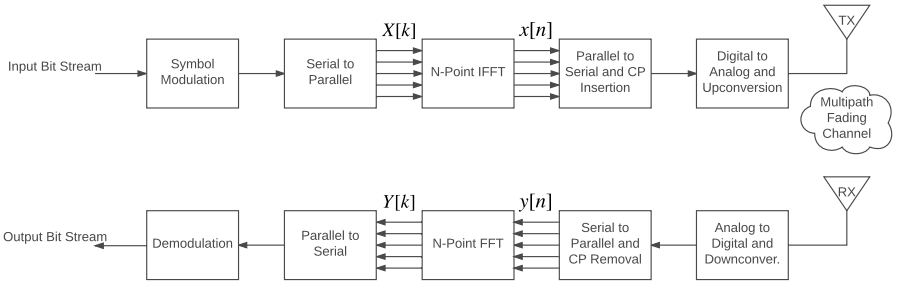

Figure 2.1: OFDM transmitter and receiver structures

The discrete-time version of an OFDM signal may be written in terms of the Discrete Fourier Transform . Consider an OFDM signal sampled with sampling frequency $F_s = 1/T_s = N\Delta f$ for some positive integer $N \gg N_{sc}$, i.e.

$$x[n] = \frac{1}{\sqrt{N}} x(nT_s) = \frac{1}{\sqrt{N}} \sum_{k=0}^{N_{sc}-1} X[k] e^{\frac{j2\pi kn}{N}} = \frac{1}{\sqrt{N}} \sum_{k=0}^{N-1} X'[k] e^{\frac{j2\pi kn}{N}} \tag{2.4}$$

where

$$X'[k] = \begin{cases} X[k], & k = 0, ..., N_{sc} - 1 \\ 0, & k = N_{sc}, ..., N - 1 \end{cases} \tag{2.5}$$

is a zero padded version of $X[k]$. Equation (2.4) says that $x[n]$ is in fact the inverse DFT of $X'[k]$. The scaling factor $1/\sqrt{N}$ has been added to achieve a unitary transform.

The fact that we can express an OFDM signal in terms of the DFT makes it convenient to implement transceiver structures using the Fast Fourier Transform (FFT) algorithm, which is illustrated in Figure 2.1.

The transmitted OFDM data can be visualized in terms of a time-frequency grid, such as in Figure 2.2. In 3GPP NB-IoT, the transmitted data is mapped to so called Resource Elements (REs), which consist of one symbol l by one subcarrier k. A subcarrier spacing of $\Delta f = 15$ kHz is used and each symbol is $1/14$ ms long in time[1]. The time domain is divided into different units: seven symbols make up one slot, two slots make up one subframe and 10 subframes make up one frame. In other words, one subframe is corresponds to 1 ms of time data. In NB-IoT, 12 subcarriers is always used, which corresponds to a total bandwidth of 180 kHz. The smallest unit of REs that can be allocated is one slot by 12 subcarriers and is denoted as a Resource Block (RB) [13].

The system sampling frequency is implementation specific and may vary between different UEs. Since low device complexity is of high importance, it is preferred to not use a higher sampling frequency than necessary. From here on, we will assume that the UE is using $F_s = 1.92$ MHz, which corresponds to an FFT size of $N = 128$. However, as we will see later, the low sampling frequency will severely impact the positioning accuracy.

[1] Throughout this thesis, normal CP is assumed

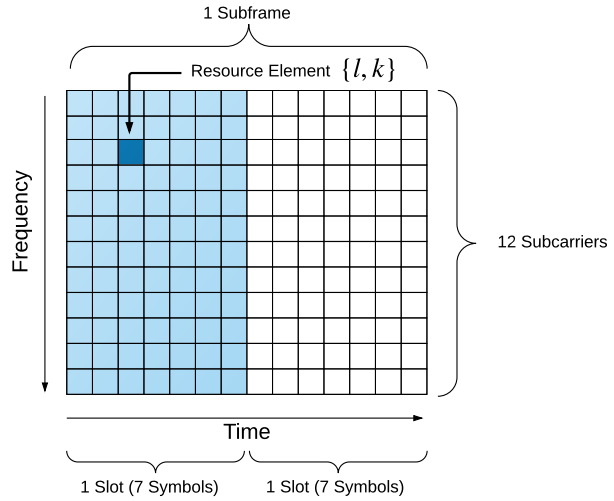

Figure 2.2: OFDM time-frequency grid showing 14 symbols by 12 subcarriers. The shaded area corresponds to one RB.

2.4 Overview of Positioning Methods in Cellular Networks

There are a number of available methods for position estimation in cellular networks. In general, the goal is to find the geometric coordinates, i.e. latitude and longitude [2], of the UE, given the location of several base stations (BSs) and some type of measurements. There are many location based services, such as fleet management, network capacity planning, tracking services, enhanced 911, and navigation tools, that utilize the user position. Some services, like street navigation, require a very accurate position estimate that is difficult to achieve without the assistance of satellite data. However, for other services where the position accuracy is not as critical, methods based on cellular measurements are sufficient. These methods rely on measurements on transmitted reference signals together with known BS locations and can be either UE-based or network-based, depending on whether the positioning estimations are carried out by the UE or the BSs. Furthermore, a method is denoted as UE-assisted if the measurements are made at the UE and reported to the network, which then calculates the position based on these measurements and the known geometric locations of the detected BSs.

The most common cellular positioning methods are based on one, or a combination of, the following measurements: received signal strength (RSS), angle of arrival (AOA), time of arrival (TOA) and time difference of arrival (TDOA) [14]. RSS measurements can be directly related to range measurements via a path loss model. Similarly, TOA measurements can be related to range, given that the UE clock is synchronized with the BSs. TDOA overcomes this requirement by forming the difference between several TOA measurements, thus eliminating the

[2] In some applications it might be beneficial to estimate the altitude as well, but for most purposes a flat geography can be assumed.

unknown signal transmit time. The observed ranges, or range differences, can then be mapped to a UE position using multilateration techniques. At least three BSs are needed for unique solution. AOA-based methods work in a similar fashion, where measured angles are mapped to a position using multiangulation. Only two BSs are needed to obtain a unique solution, but an antenna array is needed to perform measurements, which makes it less useful as a UE-assisted option [15].

In 3GPP LTE, three independent positioning techniques are supported: Assisted Global Navigation Satellite System (A-GNSS), Enhanced Cell-ID (E-CID) and OTDOA. It has been decided that Release 14 NB-IoT will support E-CID and UE-assisted OTDOA-based positioning in a similar fashion as LTE by introducing a new reference signal. TDOA will also be supported using uplink measurements, given that it uses the same NB-IoT transmissions as in Release 13 [10]. In this thesis, the scope is limited to OTDOA-based positioning, which is described in more detail in the next chapter.

Chapter 3

OTDOA-Based Positioning for NB-IoT

The basic principles of OTDOA-based positioning is illustrated in Figure 3.1. Several time synchronized BSs, in 3GPP LTE denoted as evolved Node Bs (eNodeBs), simultaneously transmit positioning reference signals. The UE detects the transmitted signals with the help of assistance data provided by a location server and estimates the TOAs, which are proportional to the distance to each eNodeB. The TOAs from neighbour eNodeBs are subtracted from the TOA of a reference eNodeB, in order to form TDOA estimates. These are then reported back to the server, which uses the measurements to calculate the UE position by multilateration. At least three TOA estimations are necessary for a unique solution.

The positioning procedure may take place either in the control plane, which carries the signaling traffic, or the user plane, which carries the data traffic. In the control plane, the positioning attempt is initiated by the the network and all the necessary reference signals and assistance data is transmitted over control channels. In the user plane, all the signalling is transmitted over bearer channels, which means that network does not distinguish it from other user data [16]. The general positioning procedures are described in the LTE Positioning Protocol, which has been updated to support NB-IoT in Release 14 [17].

3.1 Narrowband Positioning Reference Signal

The Narrowband Positioning Reference Signal (NPRS) is defined in [18]. It consists of a Quadrature Phase Shift Keying (QPSK) modulated pseudo random sequence that is mapped to REs in one subcarrier with $N_{\text{sym}} = 14$ OFDM symbols. The sequence is generated as

$$z_{n_s,l}[m] = \frac{1}{\sqrt{2}}(1 - 2c[2m]) + j\frac{1}{\sqrt{2}}(1 - 2c[2m+1]), \quad m = 0, 1 \tag{3.1}$$

where n_s is the slot number, l is the OFDM symbol number within the slot and $c[m]$ is a length-31 Gold sequence that is initialized with the seed

$$c_{\text{init}} = 2^{28}\left\lfloor \frac{N_{\text{ID}}}{512} \right\rfloor + 2^{10}\big(7(n_s+1)+l+1\big)\big(2(N_{\text{ID}} \bmod 512)+1\big) + 2(N_{\text{ID}} \bmod 512) + N_{\text{CP}} \tag{3.2}$$

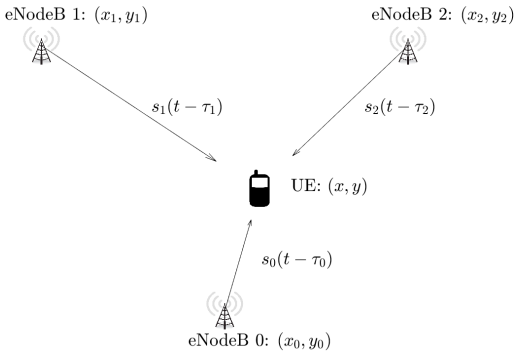

Figure 3.1: Basic principles of OTDOA-based positioning. Each eNodeB transmits a reference signal that will arrive with different time delays at the UE. The difference between the estimated time of arrivals are then used to calculate the UE position.

at the start of each OFDM symbol and N_{ID} is the physical cell identity of the eNodeB and $N_{\text{CP}} = 1$ for normal cyclic prefix. Gold-codes exhibit excellent cross-correlation properties, i.e. they are highly correlated with themselves, whereas codes with different initialization seeds have low correlation. In practice, this means that NPRS signals from different cells will be quasi-orthogonal to each other, which makes it easier for the UE to tell them apart.

The mapping of the NPRS sequence to the REs $\{l, k\}$ is shown in figure 3.2. In general, the sequence is mapped as

$$S_l[k] = z_{n_s,l}[m] \tag{3.3}$$

where

$$k = 6m + (6 - l + v_{\text{shift}}) \bmod 6 \tag{3.4}$$

$$m = 0, 1 \tag{3.5}$$

$$v_{\text{shift}} = N_{\text{ID}} \bmod 6 \tag{3.6}$$

The frequency-shift parameter v_{shift} allows for up to six different cells to transmit NPRS signals on different subcarriers so that they do not overlap in the frequency domain. This is implemented in order to minimize the interference between NPRS signals from different cell towers and together with the code orthogonality it gives the signals good hearability properties.

For in-band operation, the following symbols are allocated for NPRS transmission:

$$l = \begin{cases} 3, 5, 6, & n_s \bmod 2 = 0 \\ 1, 2, 3, 4, 5, 6, & n_s \bmod 2 = 1 \end{cases} \tag{3.7}$$

This corresponds to a total of $N_{\text{NPRS}} = 8$ symbols in the subframe being allocated for NPRS transmission. The other symbols are reserved for LTE cell specific

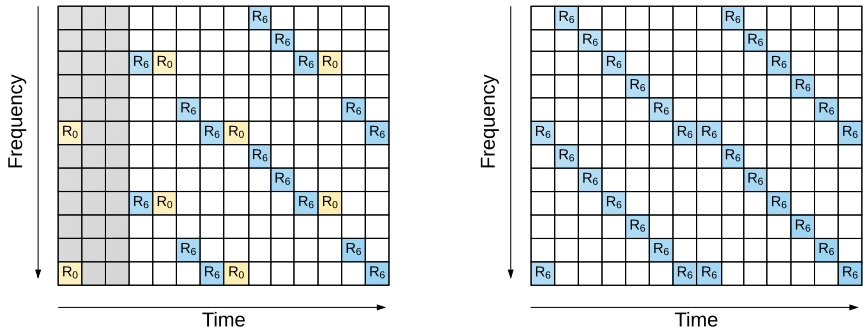

(a) In-band **(b)** Standalone

Figure 3.2: NPRS mapping to REs in one subframe, using a frequency shift $v_{\text{shift}} = 0$. The NPRS elements are denoted by R_6, the cell specific reference signal by R_0 and they shaded area is allocated to control channels. On the white REs, no data is being transmitted.

reference signal and control channels. For standalone operation, this does not need to be taken into account and therefore all the OFDM symbols can be used for NPRS transmission, such that $N_{\text{NPRS}} = N_{\text{sym}} = 14$.

The time domain symbols $s_{p,l}[n]$, where p denotes the eNodeB index, is transmitted by OFDM modulation at each cell according to (2.4), which gives

$$s_{p,l}[n] = \frac{1}{\sqrt{N}} \sum_{k=0}^{N-1} S'_{p,l}[k] e^{\frac{j2\pi kn}{N}} \tag{3.8}$$

where $S'_{p,l}[k]$ is the zero padded version of $S_l[k]$ for cell p.

3.2 Signal Model

We consider the problem where a UE located at position (x, y) receives simultaneously transmitted NPRS signals from $p = 0, ..., P-1$ eNodeBs located at positions (x_p, y_p). Without loss of generality, we assume that the signals are transmitted at time $t = 0$. From the provided assistance data, the number of participating eNodeBs P is known at the UE, but since the UE clock is not necessarily synchronized with the network, the NPRS transmit time is considered unknown. The signal from cell p will be transmitted with transmit power G_p, experience a path loss α_p, and pass through a multipath fading channel with $i = 0, ..., L_p - 1$ paths. If the signal from the ith path of the pth cell arrives at the UE at time $\tau_{p,i}$, the time of arrival in terms of samples will be

$$n_{p,i} = \lfloor \tau_{p,i} F_s \rfloor \tag{3.9}$$

where $F_s = 1.92$ MHz is the industry standard UE sampling frequency. The line-of-sight (LOS) components $\tau_{p,0}$, i.e. the first paths of arrival that propagate in a straight path from the cell tower to the UE without being scattered, are related to the UE position as $\tau_{p,0} = r_p/c$, where c is the speed of light and $r_p = \sqrt{(x - x_p)^2 + (y - y_p)^2}$ is the distance between cell-tower p and the UE.

The symbol arriving at the UE may then be modelled as

$$y_{p,i}[n + lM] = \begin{cases} 0, & 0 \leq n < n_{p,i} \\ \sqrt{\frac{G_p}{\alpha_p}} h^l_{p,i}[n] s_{p,l}[n - n_{p,i}], & n_{p,i} \leq n < n_{p,i} + M \\ 0, & n_{p,i} + M \leq n < n_{p,i} + M + \tilde{M} \end{cases} \tag{3.10}$$

for some unknown complex channel coefficients $h_{p,i}[n]$ and where M is the symbol length and $\tilde{M}$ is the size of the TOA search window. For NB-IoT systems, the symbol length M is 137 samples including CP, except for the first symbols in each slot, which are 138 samples long. The search window length $\tilde{M}$ defines the maximum TOA that can be detected and can be modified at the UE.

The path loss α_p is commonly modelled with a log-distance model [12], which in dB-scale can be written as

$$\left(\alpha_p\right)_{\text{dB}} = \left(\alpha_{p,0}\right)_{\text{dB}} + 10\gamma \log_{10} r_p + \beta_p \tag{3.11}$$

where r_p is the distance between the UE and cell tower p, $\alpha_{p,0}$ is the path loss at the reference distance, γ is the path-loss exponent, and β_p is a zero-mean Gaussian random variable that models the slow fading of the channel. Slow fading may occur due to shadowing, i.e. when the path between the cell tower and UE is obstructed by some large object.

The channel characteristics depend on the physical environment and each multipath component arises when the signal is scattered on surfaces, for example buildings in an urban environment. In OTDOA scenarios, we are only interested in finding the LOS component. In some scenarios, this component might be weaker than the scattered components or not even present at all, which makes TOA estimation difficult. 3GPP channel models are defined by a number of channel taps with corresponding tap delays and relative power. For example, the extended typical urban (ETU) channel is specified in table 3.1. Here the first three paths are weaker than the fourth, fifth, and sixth path, which will make it difficult for the UE to detect the LOS component. The UE movement is typically also modelled into the channel by specifying a maximum Doppler shift. Furthermore, since the UE is not perfectly synchronized in frequency with all cell towers, each received signal will also experience a phase rotation caused by the residual carrier frequency offset (CFO) of each cell. However, this phase does not show up explicitly if it is modelled into the channel coefficients.

The UE will receive data during a time period corresponding to the duration of one subframe plus the length of the TOA search window. The signal recorded by the UE can thus be written as

$$y[n] = \sum_{p=0}^{P-1} \sum_{l=0}^{N_{\text{sym}}-1} \sum_{i=0}^{L_p-1} y_{p,i}[n + lM] + w[n] \tag{3.12}$$

Table 3.1: ETU channel model [19]

Excess tap delay [ns]	Relative power [dB]
0	-1
50	-1
120	-1
200	0
230	0
500	0
1600	-3
2300	-5
5000	-7

where $w[n]$ is zero-mean additive white Gaussian noise (AWGN) with variance σ^2, which models the thermal noise in the receiver.

3.3 TOA Estimation

From the UE perspective, the goal is to estimate the delays $n_{p,0}$ of the first path from each cell. Since we are only interested in the OFDM symbols carrying NPRS data, we introduce the notation $\tilde{l}(s)$ $(0 \leq s \leq N_{\text{NPRS}} - 1)$ for the sth symbol containing NPRS. The UE is assumed to know this sequence a priori, since it knows if the carriers are deployed in-band or in standalone operation through initial acquisition. If we consider an AWGN channel without CFO, i.e. $h^l_{p,i} = 0$ for $i \neq 0$ and $h^l_{p,0} = 1$ $\forall p, l$, and we assume that the signals from interfering cells can be modelled as Gaussian noise, the maximum likelihood (ML) estimator of the TOA (in terms of samples) of the pth cell is the delay that maximizes the average of the symbol-by-symbol cross-correlation functions [20]:

$$\hat{n}_{p,0} = \arg\max_n \Big| \sum_{s=0}^{N_{\text{NPRS}}} R_{p,\tilde{l}(s)}[n] \Big| \tag{3.13}$$

where the symbol-by-symbol cross-correlation functions are calculated as

$$R_{p,l}[n] = \frac{1}{M} \sum_{m=n}^{n+M-1} y[m + lM] s^*_{p,l}[m - n], \quad n = 0, ..., \tilde{M} \tag{3.14}$$

In other words, the received signal is correlated with the known NPRS sequence and the delay is found where there is a peak in the correlation. In order to make sure that an actual peak is present in the correlation, the peak to average (PAR) is calculated and compared with a predefined threshold η. Here, the PAR is given

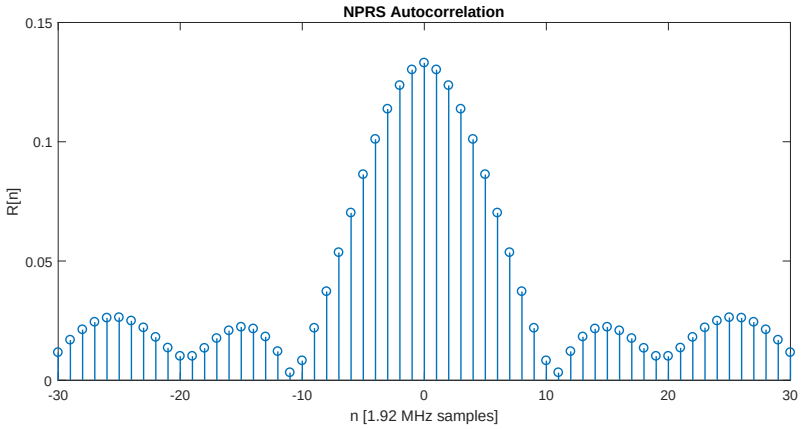

Figure 3.3: The NPRS autocorrelation function sampled at 1.92 MHz. The wide main-lobe arises due to oversampling.

by

$$\mathrm{PAR} = \frac{\left| \sum_{s=0}^{N_{\mathrm{NPRS}}-1} R_{p,\tilde{l}(s)}[\hat{n}_{p,0}] \right|}{\frac{1}{\tilde{M}} \sum_{n=0}^{\tilde{M}} \left| \sum_{s=0}^{N_{\mathrm{NPRS}}-1} R_{p,\tilde{l}(s)}[n] \right|} \tag{3.15}$$

If PAR $< \eta$, it is said that the peak is not significantly larger than what can be expected from a noise-like signal and therefore the measurement is thrown away. The choice of η will therefore correspond to a false alarm/missed detection probability.

This detection procedure is then repeated for all P cells. The assistance data provides a search window for the TOAs, so that the search can be limited to delays $n \leq \tilde{M}$. Since the NPRS signal has good correlation properties, this peak can be detected even under poor noise conditions. Figure 3.3 shows the peak of the NPRS autocorrelation function sampled at 1.92 MHz ($N = 128$). The peak has a width of ± 8 samples, which is due to the fact that the signal is oversampled (the IFFT has been zero-padded). Finally, the TOA estimates in seconds are simply given by

$$\hat{\tau}_{p,0} = \frac{\hat{n}_{p,0}}{F_s} \tag{3.16}$$

The estimator in (3.13) is the simplest form of TOA estimator and can be used as a benchmark for comparisons. However, in most realistic scenarios this estimator performs poorly. The inter-cell interference will make it difficult to detect the peak from weak cells and the CFOs will introduce a phase shift that distorts the correlations. Moreover, in multipath fading channels, the correlation will have multiple peaks, which makes it difficult to distinguish the LOS component. Therefore, more advances estimation techniques are necessary in order to increase the TOA accuracy, some of which will be discussed in section 3.6.

3.4 The Navigation Solution

Since the signal transmit times are unknown, the TOAs cannot be used directly to calculate the user position. Therefore, once the TOA estimates $\hat{\tau}_{p,0}$ are known, the TDOA estimates $\Delta\hat{\tau}_p$ are calculated by subtracting the TOA of the reference cell $p = 0$ from all the other detected TOAs:

$$\Delta\hat{\tau}_p = \hat{\tau}_{p,0} - \hat{\tau}_{0,0}, \quad p = 1, ..., P-1 \tag{3.17}$$

The TDOAs can either be reported to the network which then calculates the UE position by solving the OTDOA equations for (x, y):

$$\begin{cases} c\Delta\hat{\tau}_1 & = \sqrt{(x-x_1)^2 + (y-y_1)^2} - \sqrt{(x-x_0)^2 + (y-y_0)^2} \\ c\Delta\hat{\tau}_2 & = \sqrt{(x-x_2)^2 + (y-y_2)^2} - \sqrt{(x-x_0)^2 + (y-y_0)^2} \\ & \vdots \\ c\Delta\hat{\tau}_{P-1} & = \sqrt{(x-x_{P-1})^2 + (y-y_{P-1})^2} - \sqrt{(x-x_0)^2 + (y-y_0)^2} \end{cases} \tag{3.18}$$

The eNodeB antenna coordinates (x_p, y_p) are provided by assistance data and are assumed to be known with good precision. Geometrically, each equation in the system (3.18) corresponds to a hyperbola and the UE position is found at their intersection. In a good cell geometry where two hyperbolas do not intersect more than once, there is a unique solution for $P = 3$ and for $P > 3$ it can be solved in the least squares (LS) sense. In general, having more equations will decrease the variance of the position error, which is why it is preferable to have more than 3 eNodeBs participating in the positioning attempt. If $P < 3$, there is no unique solution and the positioning procedure fails [16].

There is no closed form solution to in (3.18), but the system can be solved by numerical methods, for example the Gauss-Newton algorithm, which is used throughout this thesis [21]. Different methods vary in terms of complexity, stability and convergence. In this thesis, however, only UE-assisted positioning is considered, so this topic will not be covered.

3.5 General Positioning Procedures

The LTE positioning protocol procedures can be summarized as follows [17]

1. The location server requests the UE positioning capabilities for OTDOA.
2. The UE responds with the OTDOA mode support (e.g. UE assisted), the supported frequency bands and whether inter-frequency measurements are supported.
3. The location server then provides the UE with assistance data, containing the cell IDs of the of the anchor cell and reference cells, expected TOAs and their uncertainty, the NPRS configuration index, the number of consecutive NPRS subframes transmitted, and other optional information.
4. The location server requests the location information from the UE with a required maximum response time.

5. The UE performs TOA measurements and responds with the results before the maximum response time has expired.

The maximum response time is given by [22]

$$T_{\text{response}} = T_{\text{NPRS}}(M-1) + 160\lceil \frac{P}{M} \rceil \quad \text{ms} \tag{3.19}$$

where T_{NPRS} is the NPRS subframe period, which is specified by higher layers, and M is the number of positioning occasions. The maximum response time is therefore at least 160 ms per positioning occasion.

3.6 Accuracy of OTDOA-based Positioning and Previous Work

There are several factors that influence the accuracy of the described method. One of them is the measurement geometry, which depends on the relative location of the eNodeBs and the UE. For example, if three eNodeBs are used, the best measurement scenario is if they form an equilateral triangle with the UE in the center [16]. If the UE is located close to the edge of the triangle formed by the eNodeBs, the dilution of precision is increased and the position estimate variance will increase. Note that this is a purely geometrical property that cannot be overcome by increased measurement precision. Therefore, this problem is not of interest from the UE point of view. Examples of other such factors that influence the accuracy of the navigation solution are eNodeB synchronization errors and errors in the eNodeB antenna coordinates (x_p, y_p) provided in the assistance data.

The errors that can be mitigated by the UE are related to the TOA estimation, since errors in $\Delta\hat{\tau}_p$ will be reflected in the position estimate. As was mentioned in section 3.3, the radio propagation environment will have a severe impact on the TOA estimates. Furthermore, interference between cells can severely reduce the hearability of the transmitted signals and must be solved using some interference mitigation technique. If the UE is located very close to one cell tower, the strong interference from this cell will make it very difficult to hear the other cells. This is known as the near-far problem and due to the large cell-sizes supported in NB-IoT, this will be crucial for succesful positioning. If the the number of participating eNodeBs and the NPRS sequences are known, the interference can be mitigated by performing successive interference cancellation (SIC). Such an approach has been implemented together with a CFO compensation in [23] and it was shown to significantly reduce the TOA errors, but only in an AWGN channel. In order for the estimation to work in realistic scenarios, channel estimation (CE) must also be done. There has been lots of research completed on OFDM channel estimation, but many estimators are unsuitable for low-end IoT applications. Furthermore, the problem of detecting weak LOS components in urban scenarios also needs to be addressed. This has been done by using an adaptive threshold in [24] and by an iterative search technique in [25]. The new proposed algorithm that is presented in the next chapter combines a low-complexity CE with CFO compensation and SIC together with either one of these first path detection methods.

Due to the time-frequency uncertainty principle, OTDOA positioning is especially difficult for a narrowband system like NB-IoT (the NPRS signal is transmitted at a bandwidth of 180 kHz). If the UE oversamples the signal at 1.92 MHz,

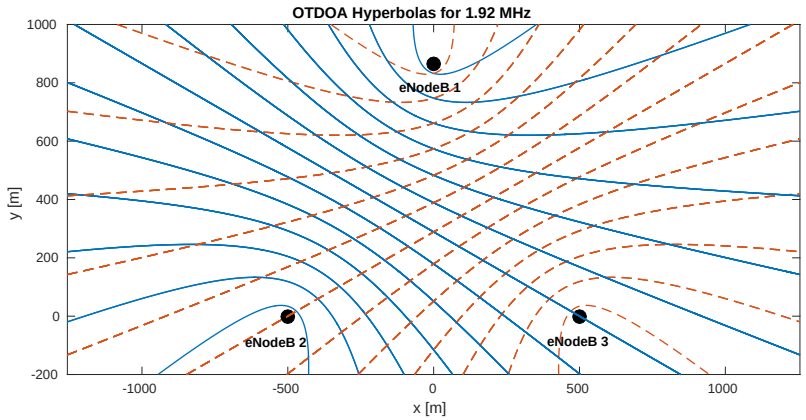

Figure 3.4: Discretization of UE locations. The solid lines represent hyperbolas corresponding to $\Delta\tau_1$ and the dashed lines hyperbolas corresponding to $\Delta\tau_2$. The intersection between the hyperbolas are possible solutions to the OTDOA equations at 1.92 MHz resolution

more accurate TOA estimation is possible, but performance is still bandwidth limited. Yet, even at this sampling rate, the signal travels approximately 150 m per sampling period. Consequently, the time discretization caused by sampling in practice also discretizes the coordinates grid. In standard LTE, sampling rates up to 30.72 MHz are used, which makes very accurate positioning possible. On the other hand, at 1.92 MHz it is very difficult to achieve accurate positioning, even if all the TOAs are perfectly estimated to the nearest sample.

Figure 3.4 illustrates the coordinate discretization caused by the low sampling rate. Three eNodeBs have been placed in an equilateral triangle with coordinates $(0, \sqrt{3}d/2)$, $(-d/2, 0)$ and $(d/2, 0)$. Using this geometry, the hyperbolas for all combination of arrival times $\hat{\tau}_{p,0} = 0, T_s, ..., 6T_s$ have been calculated and plotted. The corresponding UE positions are found at the intersections between these hyperbolas and as can bee seen, this is a very rough discretization where in some places, especially where the dilution of precision is high, the distance between possible UE positions is over 100 m. In order to work around this problem, the TOAs need to be estimated with sub-sample precision. Such approaches have been implemented in [23, 26] and it has been shown to give significant performance increases. Therefore, in the proposed algorithm presented in the next chapter, the sub-sample TOA estimation is combined with the other techniques in order to further improve the positioning accuracy.

Chapter 4

Proposed EM-SIC Algorithm

In this chapter, a novel algorithm based on expectation maximization channel estimation and successive interference cancellation (EM-SIC) is presented. The algorithm consists of two stages that are presented below. In the first stage, the TOA of the strongest path of each cell is estimated using a coherent summation of symbol-by-symbol cross-correlations. Then a simple channel estimation for this path is performed, such that it can be removed from the input data before moving on to the next cell. This stage can be repeated N_{iter} iterations before moving to the second stage, which consists of performing sub-sample TOA estimation by interpolating the correlation around the coarse peak estimation. This is combined

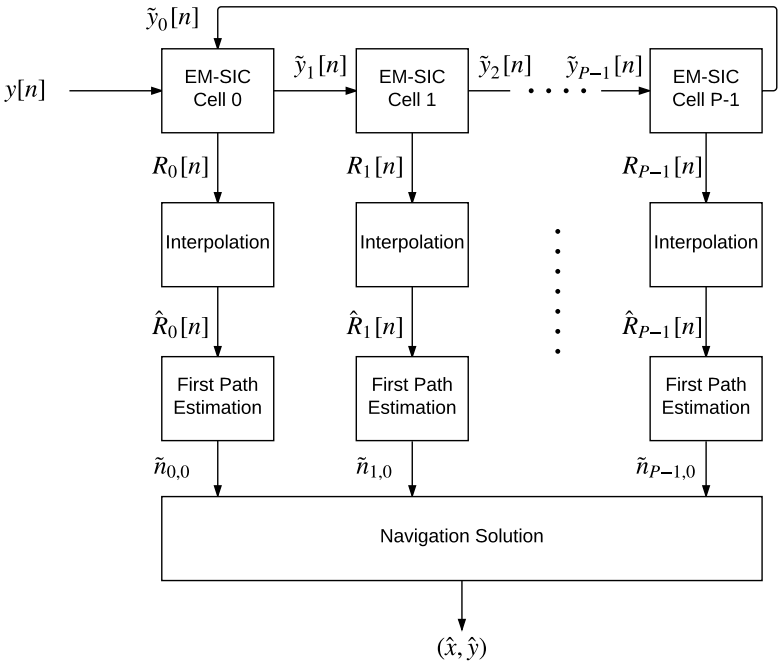

Figure 4.1: Block diagram description of the proposed algorithm.

with an iterative first path estimation procedure in order to combat multipath interference. A block diagram showing a simplified version of the whole algorithm is presented in Figure 4.1.

4.1 EM-SIC Strongest Path Estimation

In Figure 4.2 a more detailed version of the EM-SIC block for one cell is shown. Using the recorded input data, the symbol-by-symbol cross-correlations are calculated according to (3.14). In order to achieve a low-complexity algorithm, it is assumed that the channel for each path is constant over one subframe due to the low mobility of NB-IoT UEs and that each sample is shifted by a phase rotation caused by the residual CFO ϵ_p, i.e.

$$h_{p,i}^{l}[n] = h_{p,i} e^{j2\pi \frac{\epsilon_p (n+lM)}{N}} \tag{4.1}$$

Moreover, channel estimation will only be performed for the strongest path, since the low UE sampling rate makes it difficult to resolve the different multipath components.

4.1.1 Residual CFO Estimation

If there is a residual CFO present in the signal, this needs to be corrected before the correlations can be summed coherently. In order to simplify calculations, we assume that the CFO is relatively small, such that the correlations can be coherently added within one OFDM symbol. The best linear unbiased estimator for the CFO is described in [27] and reads

$$\tilde{\epsilon}_p[n] = \sum_{m=1}^{4} w(m)\phi(m,n) \tag{4.2}$$

where

$$\phi(m,n) = \frac{N}{2\pi M(N_{\mathrm{NPRS}} - m)} \sum_{s=0}^{N_{\mathrm{NPRS}}-m-1} \frac{\arg\left\{R_{p,\tilde{l}(s)}[n] R^{*}_{p,\tilde{l}(s+m)}[n]\right\}}{\tilde{l}(s+m) - \tilde{l}(s)} \tag{4.3}$$

Here the $\arg\{\cdot\}$ operation returns the angle in the range $[-\pi, \pi)$ and the combing coefficients $\mathbf{w} = [w(1), ..., w(4)]$ are calculated according to [27, eq. 16], which yields

$$\mathbf{w} = [0.4762, 0.3095, 0.1667, 0.0476] \tag{4.4}$$

By correcting for the CFO, the symbol-by-symbol correlations may now be added coherently:

$$R_p[n] = R_{p,\tilde{l}(0)}[n] + \sum_{s=1}^{N_{\mathrm{NPRS}}-1} e^{-j2\pi\tilde{\epsilon}_p[n]\frac{M\left(\tilde{l}(s)-\tilde{l}(0)\right)}{N}} R_{p,\tilde{l}(s)}[n] \tag{4.5}$$

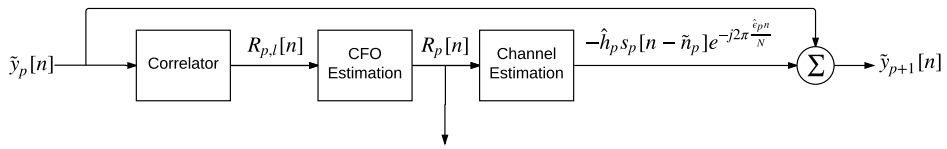

Figure 4.2: Detailed block diagram description of the EM-SIC process for cell p

Using the total correlation, the TOA $\tilde{n}_p$ of the strongest path of the pth cell is found where the correlation has its peak:

$$\tilde{n}_p = \arg\max_n |R_p[n]| \tag{4.6}$$

and the residual CFO is set to

$$\hat{\epsilon}_p = \tilde{\epsilon}[\tilde{n}_p] \tag{4.7}$$

The TOA is stored if PAR $> \eta$, otherwise it is thrown away and the algorithm moves on to the next cell without performing interference cancellation.

4.1.2 Channel Estimation and Interference Cancellation

With the assumption that the channel is constant over the whole subframe, the channel coefficient for the strongest path of the pth cell can be estimated as

$$\hat{h}_p = \frac{1}{MN_{\mathrm{NPRS}}} \sum_{s=0}^{N_{\mathrm{NPRS}}-1} \sum_{k=\tilde{n}_p}^{\tilde{n}_p+M-1} \frac{y[k+\tilde{l}(s)M]}{s_{p,\tilde{l}(s)}[k-\tilde{n}_p]} e^{-j2\pi\frac{\hat{\epsilon}_p(k+\tilde{l}(s)M)}{N}} \tag{4.8}$$

where without loss of generality we have assumed that $s_{p,\tilde{l}(s)}[n] \neq 0, \forall n$. The channel estimate is then updated with a linear minimum mean square error (LMMSE) filter:

$$\tilde{h}_p = \frac{\hat{h}_p}{1+\hat{\sigma}_p^2/|\hat{h}_p|^2} \tag{4.9}$$

where the noise variance estimate is given by

$$\hat{\sigma}_p^2 = \frac{1}{MN_{\mathrm{NPRS}}} \sum_{s=0}^{N_{\mathrm{NPRS}}-1} \sum_{k=\tilde{n}_p}^{\tilde{n}_p+M-1} \left| y[k+\tilde{l}(s)M] - s_{p,\tilde{l}(s)}[k-\tilde{n}_p] e^{-j2\pi\frac{\hat{\epsilon}_p(k+\tilde{l}(s)M)}{N}} \right|^2 \tag{4.10}$$

Using the channel coefficient estimate $\tilde{h}_p$, the CFO estimate $\hat{\epsilon}_p$ and the TOA estimate $\tilde{n}_p$, interference cancellation can be performed by subtracting perturbed versions of the NPRS symbols $s_{p,l}[n]$ from the input data. When moving to the the EM-SIC block for the pth cell, the NPRS signals from all other cells are subtracted from the input data:

$$\tilde{y}_p[k+\tilde{l}(s)M] = y[k+\tilde{l}(s)M] - \sum_{q\neq p} \tilde{h}_q s_{q,\tilde{l}(s)}[k-\tilde{n}_q] e^{-j2\pi\frac{\hat{\epsilon}_p(k+\tilde{l}(s)M)}{N}} \tag{4.11}$$

For the next block, the correlation in (3.14) is computed using $\tilde{y}_p[n]$ instead of $y[n]$, and the same goes for equations (4.8)-(4.10).

The procedure is repeated for all the $P-1$ cells and then starts over again for the first cell. All the previous estimates $\tilde{h}_p$, $\hat{\epsilon}_p$, and $\tilde{n}_p$ are then recalculated. Since the new estimates are based on a signal where ideally all the interference has been removed, they are more accurate. The loop over the cells is the repeated N_{iter} times. A larger number of iterations will yield better accuracy at the cost of higher computational complexity and in general 2-3 iterations can harvest the major gains.

4.2 Resolution Refinement Through Correlation Interpolation

At the last iteration of the EM-SIC repetitions, the resolution of each TOA estimate is refined by interpolating the correlation obtained from (4.5). Here we consider interpolation by a factor V around a window of size W around the coarse TOA estimates $\tilde{n}_p$. Using sinc-function based interpolation, the refined correlations may then be written as

$$\hat{R}_p[n] = \sum_{m=\tilde{n}_p-W}^{\tilde{n}_p+W} R_p[m] \frac{\sin \pi(\frac{n}{V} - m)}{\pi(\frac{n}{V} - m)}, \quad n = -VW, ..., VW \tag{4.12}$$

For example, if we let $V = 16$, this will imply an interpolation from 1.92 MHz sampling rate to 30.72 MHz. From Figure 3.3, we also know that the window size should be at least $W = 8$ samples in order to capture the whole main lobe of the peak. In order for the interpolation to work properly, the signal to noise and interference ratio (SINR) needs to be relatively high, otherwise the noise will be interpolated rather than the signal itself. Figure 4.3 illustrates an ideal scenario at very high SINR where the TOA does not correspond to an integer number of 1.92 MHz samples. By interpolating to the higher sampling rate, the sub-sample TOA can be recovered, which is done in the next step.

4.3 Iterative First Path Estimation

In order to find the TOA of LOS component, an iterative technique for multipath interference mitigation described in [25] has been implemented in the final stage. The purpose of this step is to detect a weak LOS component which would otherwise be missed. In the first iteration we start with the original interpolated correlation $\hat{R}_{p,0}[n] = \hat{R}_p[n]$. Then TOA for the strongest NPRS component is then estimated as:

$$\tilde{n}_{p,i} = \arg\max_n |\hat{R}_{p,i}[n]| \tag{4.13}$$

This component is then subtracted from the correlation by using the ideal normalized NPRS autocorrelation function $R_0[n]$ at the estimated delay. An updated cross-correlation for the next iteration is then found as:

$$\hat{R}_{p,i+1}[n] = \hat{R}_{p,i}[n] - \hat{R}_{p,i}[\tilde{n}_{p,i}] R_0[n - \tilde{n}_{p,i}] \tag{4.14}$$

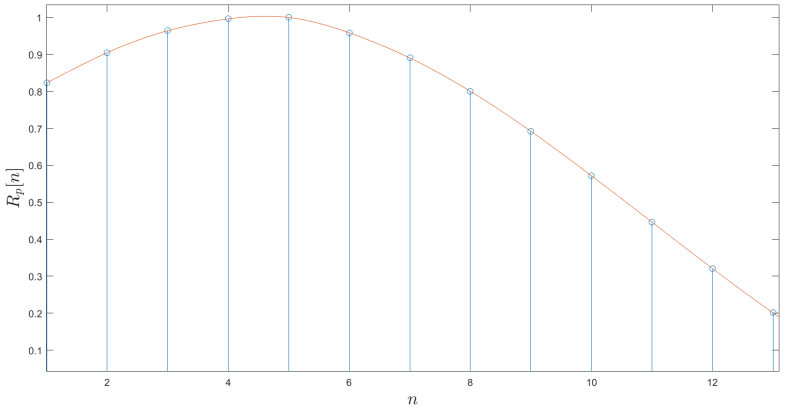

Figure 4.3: Example of the resolution enhancements obtained by interpolation of $R_p[n]$. Here the true delay τ_p does not correspond to an integer multiple of the sampling period at 1.92 MHz (in this case it lies between 4 and 5 samples) and the coarse TOA estimate will therefore result in a large rounding error. By interpolating to 30.72 MHz, the delay can be more accurately estimated.

In order to determine if there is another multipath component present, the PAR is calculated:

$$\widehat{\mathrm{PAR}}_i = \frac{\max_n |\hat{R}_{p,i}[n]|}{\frac{1}{\hat{M}} \sum_{n=0}^{\hat{M}-1} |\hat{R}_{p,i}[n]|} \tag{4.15}$$

Then, if $\widehat{\mathrm{PAR}}_i > \gamma$, for some threshold γ, the iteration continues and the TOAs $\tilde{n}_{p,i}$ of all the paths are stored. When there is only noise left in the correlation, the condition will be violated and the LOS component is estimated as the path with the smallest TOA, i.e.

$$\tilde{n}_{p,0} = \min_i \{\tilde{n}_{p,i}\} \tag{4.16}$$

This is the final TOA estimate that will be reported in order to use for the navigation solution.

4.4 Cramér-Rao Lower Bound

According the the Cramér-Rao Lower Bound (CRLB) theorem, the variance of any unbiased estimator $\hat{\theta}$ must satisfy

$$\mathrm{var}(\hat{\theta}) \geq \frac{1}{-\mathbb{E}\left[\frac{\partial^2 \ln p(x;\theta)}{\partial \theta^2}\right]} \tag{4.17}$$

where $\mathbb{E}\{\cdot\}$ denotes the expectation operator and $p(x;\theta)$ is the likelihood function of the observed variable x given θ. One way to evaluate an estimator is to see how close it can approach the CRLB. For simplicity, let us consider the the problem of estimating the arrival time $\tau_{0,0}$ of the NPRS signal from one cell in an AWGN channel without CFO, with unit transmit power, and no path loss. We can then reuse the signal model from (3.10) with $G_0 = \alpha_0 = 1$, $h^l_{0,i} = 0$ for $i \neq 0$ and $h^l_{0,0} = 1\ \forall l$ the transmit power is unity and there is no path loss. Using the observable in (3.12) with $P = 1$, the CRLB can be explicitly calculated as [26]

$$\mathrm{var}(\hat{\tau}_{0,0}) \geq \frac{\sigma^2}{8\pi^2\Delta f^2 \sum_{s=0}^{N_{\mathrm{NPRS}}-1} \sum_{k=0}^{N_{\mathrm{sc}}-1} k^2 |S_{\tilde{l}(s)}[k]|^2} = \sigma^2_{\mathrm{CRLB}} \tag{4.18}$$

Since the NPRS signal is a QPSK modulated gold sequence, $|S_l[k]| = 1$ where there is an NPRS symbol and 0 otherwise. Therefore the bound only depends on the subcarrier spacing and the distance between the occupied subcarriers and the center frequency. Since only 12 subcarriers are used in NB-IoT, this sets a much higher CRLB than for wideband signals. In section 5.6, the performance of the EM-SIC algorithm is compared to this bound under various simulation environments. Of course it is much more difficult to attain the CRLB with interference from other cells, CFO and time varying multipath fading present, but as far as the author is concerned, there is no explicit expression for the CRLB in these cases. Therefore, the bound in (4.18) will serve as a reference variance in comparisons.

4.5 Computational Complexity

The computational complexity of the proposed algorithm can be analysed by counting the number of operations carried out by each block in the algorithm. In this analysis, we will limit the scope to counting the number of complex multiplications, divisions and evaluation of trigonometric functions, such as $\sin\{\cdot\}, \cos\{\cdot\}$ and $\arg\{\cdot\}$. Note that one complex multiplication corresponds to four real multiplications.

The first correlation block requires the computation of $R_{p,\tilde{l}(s)}[n]$ for $s = 0, ..., N_{\mathrm{NPRS}} - 1$ and $n = 0, ..., \tilde{M}$, i.e. for a total of $\tilde{M}N_{\mathrm{NPRS}}$ samples. Using the explicit formula given in (3.14), this would require M complex multiplications per sample, where $M = 137$ or 138 is the symbol length in samples. However, since the cross-correlation may be written in terms of a convolution, it can be calculated more efficiently, for example using the overlap-save method [28]. This method breaks down the sequences into smaller overlapping sequences and calculates the linear convolution via several FFT and IFFT operations. With an FFT size of $N = 2^\nu$ for some integer ν, the number of complex multiplications per sample reduces to

$$\frac{N \log_2 2N}{N - M + 1} \approx \frac{2^\nu}{2^\nu - M} \tag{4.19}$$

Using this expression, we can find a value of N that minimizes the computational effort for each correlation. The same method can be applied to the interpolation

Algorithm 1 Proposed EM-SIC algorithm

$\tilde{y}_0[n] \leftarrow y[n]$
for $n_{\text{iter}} \leftarrow 1$ **to** N_{iter} **do**
  for $p \leftarrow 0$ **to** $P-1$ **do**
    calculate $R_{p,\tilde{l}(s)}[n], \forall s$ ▷ Correlator block
    calculate $\hat{\epsilon}_p, R_p[n], \tilde{n}_p$ ▷ CFO block
    if PAR $> \eta$ **then**
      calculate $\hat{h}_p, \tilde{y}_{p+1}[n]$ ▷ Channel estimation block
    else
      $\tilde{y}_{p+1}[n] \leftarrow \tilde{y}_p[n]$
    end if
    if $n_{\text{iter}} = N_{\text{iter}}$ **then**
      calculate $\hat{R}_p[n]$ ▷ Interpolation block
      $\hat{R}_{p,0}[n] \leftarrow \hat{R}_p[n]$
      $\tilde{n}_{p,0} \leftarrow \arg\max_{|} \hat{R}_{p,0}[n]|$
      while $\widehat{\text{PAR}} > \gamma$ **do** ▷ First path estimation block
        calculate $\hat{R}_{p,i+1}[n]$
        $\tilde{n}_{p,i} \leftarrow \arg\max |\hat{R}_{p,i}[n]|$
        $i \leftarrow i+1$
      end while
      $\tilde{n}_{p,0} \leftarrow \min_i \{\tilde{n}_{p,i}\}$
    end if
  end for
end for
return $\{\tilde{n}_{p,0}\}$

block, since (4.12) can also be interpreted as a convolution with a sinc-filter, but now the sequence input length is $2W+1 = 17$. The number of complex multiplications per sample for the two blocks using different FFT sizes is shown in Table 4.1. It can be seen that the correlation block achieves minimum complexity for $N = 1024$ and therefore this is the best choice of N (not considering other implementation aspects). The complexity for the interpolation block is not of as much concern, since the interpolation will be performed for less samples and will not be executed as often.

In Table 4.2, the number of operations carried out by each block has been calculated approximately. A TOA search window of $\tilde{M} = 192$ samples (0.1 ms) has been assumed, but in most scenarios this is probably larger than necessary. The calculations show that most of the computational burden lies within the correlation and CFO estimation blocks. The complexity depends asymptotically upon $\tilde{M}$ and can therefore be lowered by choosing a smaller search window. The channel estimation block is not as burdensome and its complexity depends only upon the symbol length M and the number of NPRS symbols N_{NPRS}, which are both

Table 4.1: The number of complex multiplications per sample required by the overlap-save algorithm for different FFT sizes N

N	Correlation	Interpolation
8	19.20	9.60
9	13.62	10.33
10	12.68	11.17
11	12.85	12.09
12	13.45	13.05

constant. The interpolation and first path estimation blocks are the least complex blocks, although their complexity can be modified by changing the interpolation factor V and the interpolation window W.

The total complexity of the whole algorithm can to some extent be regarded as random, since it is dependent on the received signal. In general, the complexity increases with the number of cells P and the number of iterations N_{iter}. The positioning accuracy generally also increases with P, but this is not of concern to the UE, since the number of participating eNodeBs is determined by the network. However, the number of iterations N_{iter} should be chosen as small as possible, while still achieving good TOA accuracy. Nevertheless, some blocks of the algorithm may never be executed if PAR thresholds are not met. In Algorithm 1, the outline of the whole algorithm is shown, and here we see that the channel estimation block will only be executed for cells where the correlation exceeds the PAR threshold. Similarly, the first path estimation block will keep iterating until the first path is found. The total complexity of the algorithm must therefore be evaluated statistically for different input signals. A "worst case" in terms of complexity (which is usually the best case in terms of accuracy), can be evaluated using the numbers in Table 4.2. If we assume $P = 6$ and $N_{\text{iter}} = 2$, and we assume that the channel estimation block is executed for all cells in both iterations, the total amount of complex multiplications, divisions and trigonometric evaluations become approximately 594 000, 308 000 and 358 000 respectively. This is reasonable to execute within the response time, for both hardware and software implementations. For example, assuming that the algorithm is running at a 100 MHz hardware implementation executing one operation per clock cycle, the total computational burden would be 10 ms, which is well within the response time requirement of 160 ms.

Several buffers are needed in order to store the estimated parameters in each iteration, but most of the memory consumption will be used to store the received signal and the 3-6 reference signals, which have a length up to complex 1920 samples. Assuming a 16-bit fixed point implementation, this requires memory buffers in the order of 10s of kilobytes. The buffers of other operations, such as the FFT/IFFT, should also be considered.

The scope of this thesis does not include implementation aspects and further analysis of the complexity and memory consumption for a given implementation framework is left as future work.

Table 4.2: The approximate number of complex multiplications, divisions, and trigonometric function evaluations required by each block in the proposed algorithm for $\tilde{M} = 192$, $M = 137$, $N_{\mathrm{NPRS}} = 8$, $V = 16$, $W = 8$, and FFT size $N = 1024$ for the overlap-add method, as well as the asymptotic complexity of each block. A rough estimate of the total complexity of the algorithm is given, assuming that the correlation, CFO estimation and channel estimation blocks are executed $P \times N_{\mathrm{iter}} = 12$ times, and the interpolation and first path estimation blocks $P = 6$ times.

Block	Mult.	Div.	Trig.	Asympt.
Correlation	19 500	-	-	$\mathcal{O}(\tilde{M})$
CFO Est.	26 100	24 600	27 600	$\mathcal{O}(\tilde{M})$
Channel Est.	3 800	1 100	2 200	$\mathcal{O}(1)$
Interpolation	1400	-	-	$\mathcal{O}(VW)$
First Path Est.	200 (per iter.)	-	-	$\mathcal{O}(V\tilde{W})$
Total	594 000	308 000	358 000	

Chapter 5
Numerical Simulations

5.1 Simulation Parameters

An OTDOA simulator for NB-IoT was implemented in Matlab with the purpose of demonstrating the performance increase gained by the proposed algorithm using Monte Carlo simulations. The simulator places cell sites with a specific inter-site distance in a hexagonal grid, such as in Figure 5.1. UEs are then dropped with a uniform geometric distribution inside one of the cells, in this case the one with cell ID 8. The propagation channels from each cell tower to each UE are simulated and such that unique received signals are created. The TOAs are then estimated using different methods: the standard estimate in (3.13), SIC without frequency offset compensation (FOC), SIC with FOC, SIC with FOC and interpolation, and finally using the complete proposed algorithm with SIC, FOC, interpolation and first-path estimation. This corresponds to activating and deactivating different parts of the block diagrams in Figure 4.1 and 4.2. The performance of the different methods are evaluated by calculating the TOA errors $\tau_{p,0} - \hat{\tau}_{p,0}$ and the error $\sqrt{(x-\hat{x})^2 + (y-\hat{y})^2}$ of the corresponding positioning result.

When evaluating the positioning errors, we also need to consider that not all positioning attempts are successful. For example, if the PAR threshold of a certain cell is not exceeded, the TOA for that cell will not be estimated. Since TOA estimates from at least three cells is necessary for obtaining a position estimate, some UEs will therefore not be located. Furthermore, if the position error exceeds 500 m, the estimate is not considered, since the network is assumed to have some a priori knowledge of the approximate UE location. For example, by using the cell ID, the network knows in which cell the UE is located, so if the OTDOA solution converges outside this cell, we know that the measurements cannot be trusted. Using these criteria, we define the *localizability* as the percentage of UEs that have been successfully located. This can also be interpreted as the probability of being able to successfully assign a position to a given UE.

Furthermore, the probability of detection P_d was simulated for different methods. P_d is here defined as correctly identifying the received NPRS signal from a cell within ± 1 samples at 1.92 MHz. For this type of simulation, we do not have to consider interpolation, since it will have no impact on this probability. The results are presented in section 5.2.

The TOA errors are presented in terms of its empirical probability distribution

Table 5.1: Parameters used in numerical simulations

Parameter	Value
Number of eNodeBs P	6
Number of UEs	5000 uniformly dropped
Inter-site distance d	1 732 m
Operation mode	In-band
Carrier frequency	900 MHz
Channel model	AWGN, ETU
Channel Doppler frequency	3 Hz
eNodeB-antenna	1
UE-antenna	1
Consecutive NPRS subframes	1
NPRS muting	false
UE-sampling frequency F_s	1.92 MHz
Thermal noise density	250 dB below transmit power
Shadowing standard deviation	8 dB
Inter-cell shadowing correlation	0.5
Path loss model (r_p in km)	$(\alpha_p)_{\mathrm{dB}} = 120.9 + 37.6 \log_{10} r_p$
CFO	Uniformly drawn in $\pm$500 Hz
Number of iterations N_{iter}	2
PAR threshold η	3
First path PAR threshold γ	3
TOA search window $\tilde{M}$	192 samples
Interpolation factor V	16
Interpolation window W	8

function (PDF) in section 5.3 and the positioning results in terms of its empirical cumulative distribution function in section 5.4. As it was established first-path estimation block did not affect the results in AWGN and ETU channels, the benefits of this block was analysed with a simulation using a specific two-path channel model in section 5.5. Finally, a simulation of the TOA variance compared to the CRLB is presented in section 5.6. Unless otherwise specified, the simulation parameters in Table 5.1 are used [29].

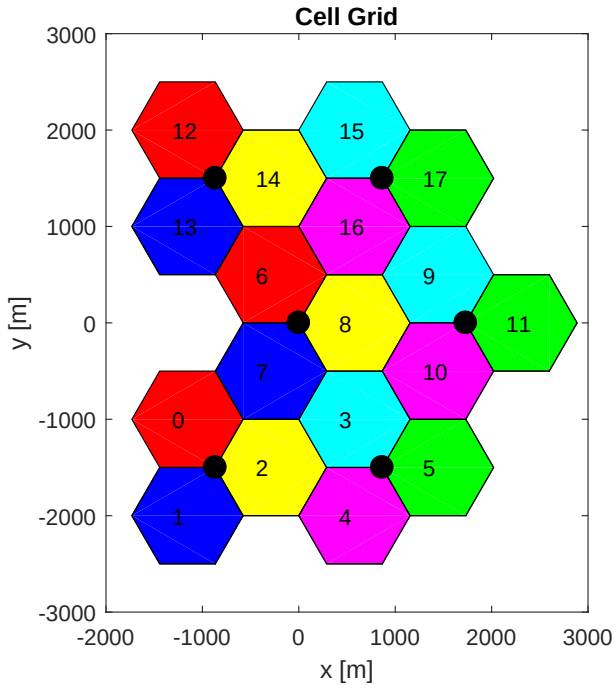

Figure 5.1: The cell grid used in the numerical simulations. The black dots indicate cell tower sites and each sector has been given a unique cell ID. In the simulations, UEs are dropped uniformly in the sector with cell ID 8.

5.2 Probability of detection

The probability of detection P_d was simulated in both AWGN and ETU channels for different noise powers. The transmit powers G_p of each cell tower were fixed and the noise power N_0 was varied between 250 and 150 dB below the transmit power (note that the SINR of each received signal is random, since it depends on the distance to each cell and the log-normal shadowing). The results are shown in Figure 5.2 and 5.3. From the results we see that using SIC and FOC increases the probability of detection in low-noise scenarios, both in the AWGN and ETU channels. However, the benefits are not as big in ETU as for AWGN.

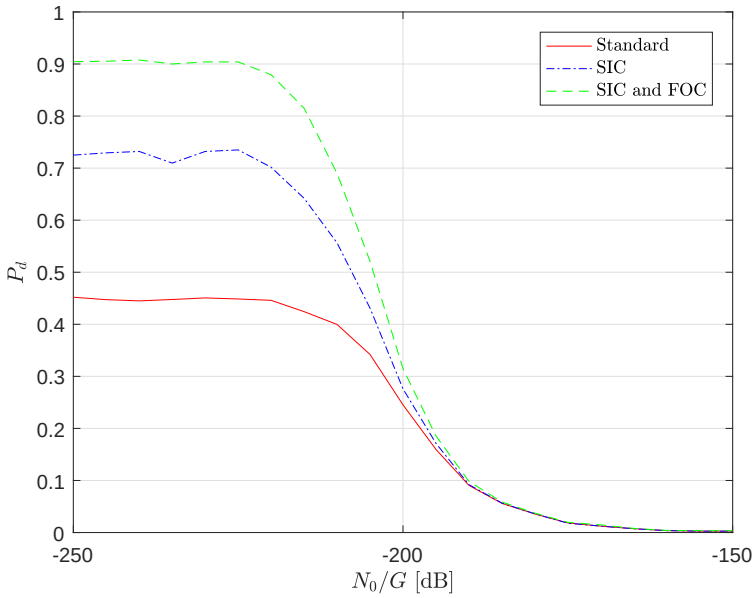

Figure 5.2: Probability of detection P_d for different noise power to transmit power ratios N_0/G in AWGN channel.

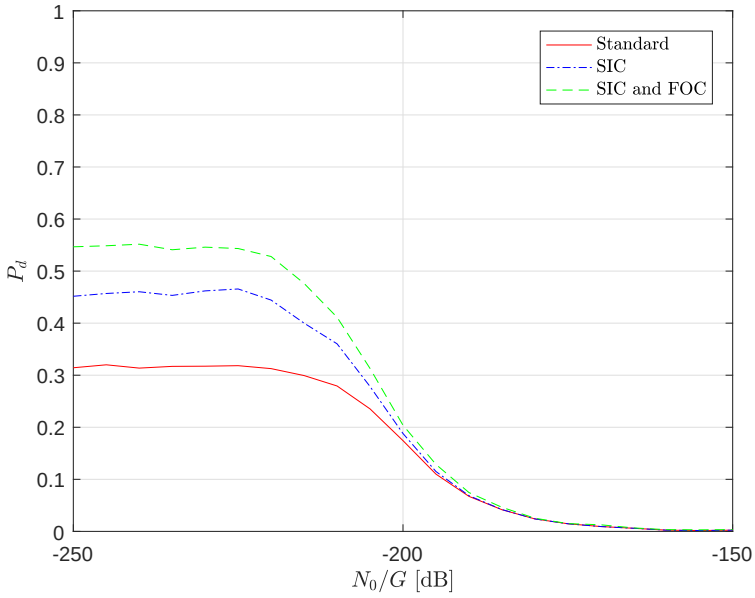

Figure 5.3: Probability of detection P_d for different noise power to transmit power ratios N_0/G in ETU channel.

5.3 TOA Errors

The TOA errors were simulated in both AWGN and ETU channels using the different techniques. The results are shown in Figure 5.4 and 5.5. Here we see that the SIC, FOC and interpolation each reduces the variance of the TOA estimates. In AWGN, the interpolation gives an especially large variance reduction. However, in ETU the benefits for each block are not as big, and the overall TOA variance is much greater than in AWGN for each method. In general, the TOA estimates are slightly biased, which is due to a simulation bug, but the bias cancels when the TDOAs are formed.

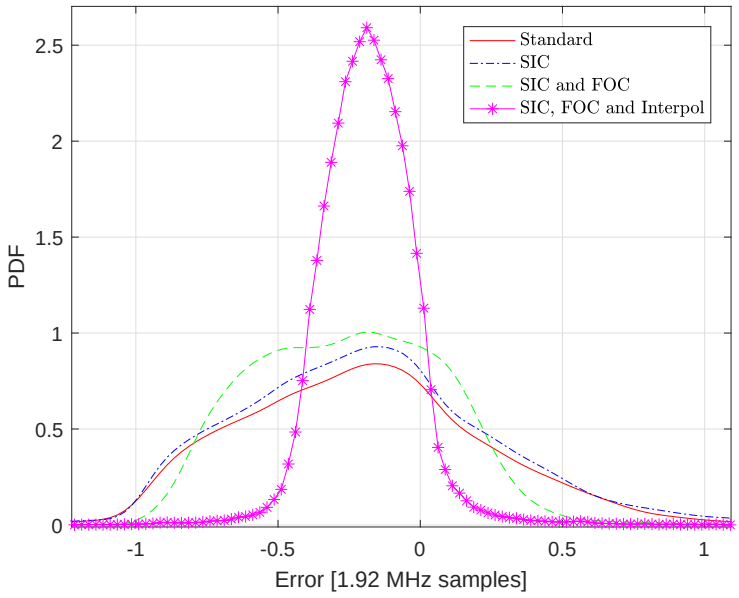

Figure 5.4: Empirical PDF of the TOA errors in the AWGN channel.

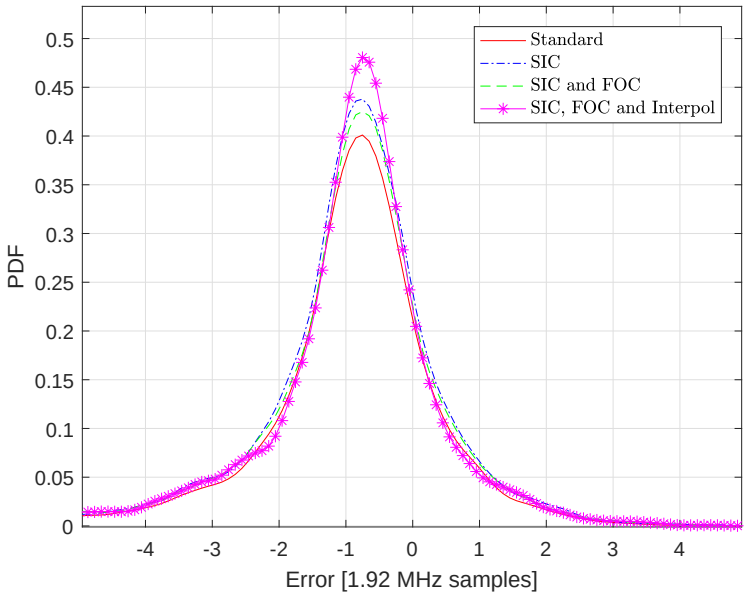

Figure 5.5: Empirical PDF of the TOA errors in the ETU channel.

5.4 Positioning Errors

The positioning errors were simulated in both AWGN and ETU channels for the different methods. The results are shown in Figure 5.6 and 5.7, together with Table 5.2 and 5.3. The proposed algorithm greatly increases the positioning accuracy as well as the localizability ratio in AWGN channel. For ETU the accuracy is only modestly increased, but the benefits are significant in terms of localizability.

In Figure 5.8, the geographic distribution of the estimated UE positions within the sector from the AWGN simulation is shown. Note that the UEs were dropped uniformly within the sector, so for a 100 % localization ratio, we would expect to see a uniform distribution. More simulation results investigating the impact of the number of cells P, the inter-site distance (between cell towers) d, the PAR threshold η and the number of SIC iterations N_{iter} are shown in Figures 5.9-5.14.

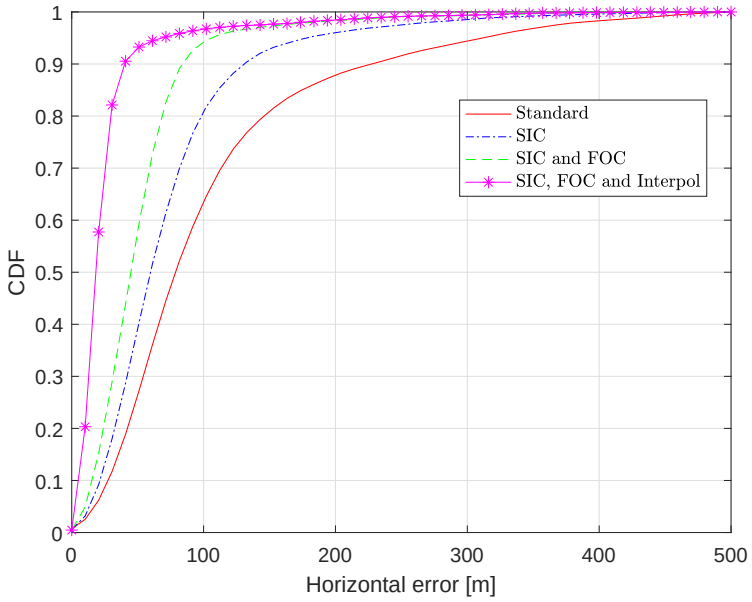

Figure 5.6: Empirical CDF of the horizontal positioning errors in AWGN channel.

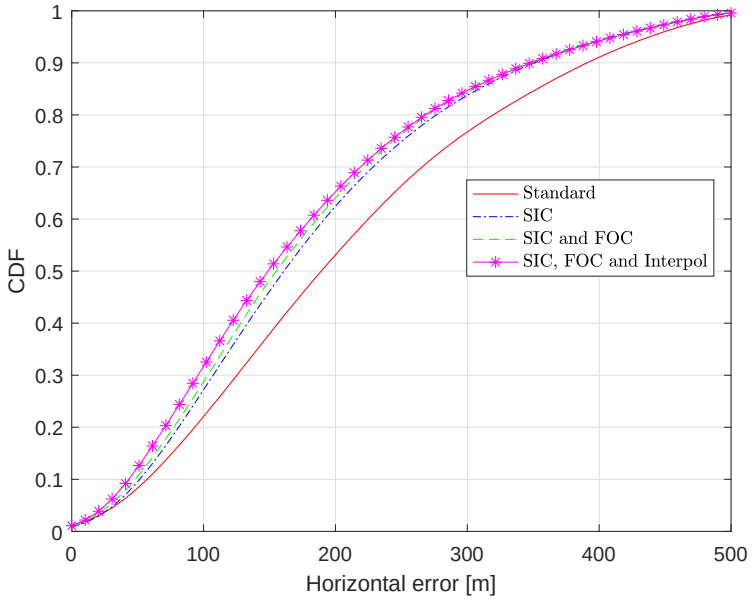

Figure 5.7: Empirical CDF of the horizontal positioning errors in ETU channel.

Table 5.2: Positioning results in AWGN

Method	95th percentile [m]	Localization ratio
Standard	342	0.67
SIC	184	0.88
SIC and FOC	97	0.97
SIC, FOC and Interpol	61	0.97

Table 5.3: Positioning results in ETU

Method	95th percentile [m]	Localization ratio
Standard	435	0.56
SIC	406	0.76
SIC and FOC	411	0.85
SIC, FOC and Interpol	409	0.86

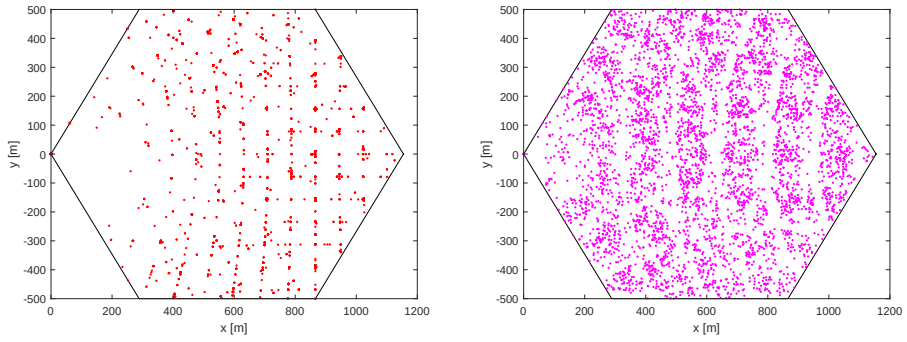

(a) Standard **(b)** SIC, FOC and Interpol

Figure 5.8: Distribution of estimated UE positions in one cell for simulation in AWGN channel using two different estimation techniques.

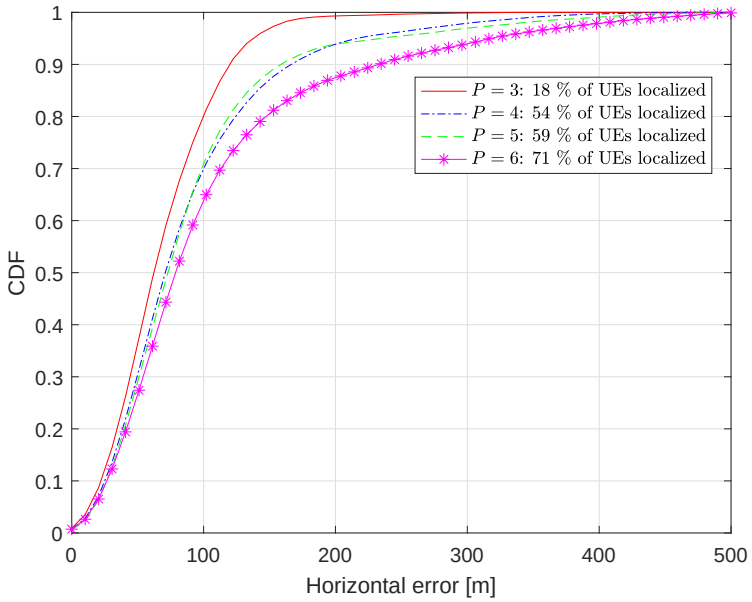

Figure 5.9: Positioning errors and localization ratios for different number of participating eNodeBs P in AWGN channel, using the standard TOA estimate.

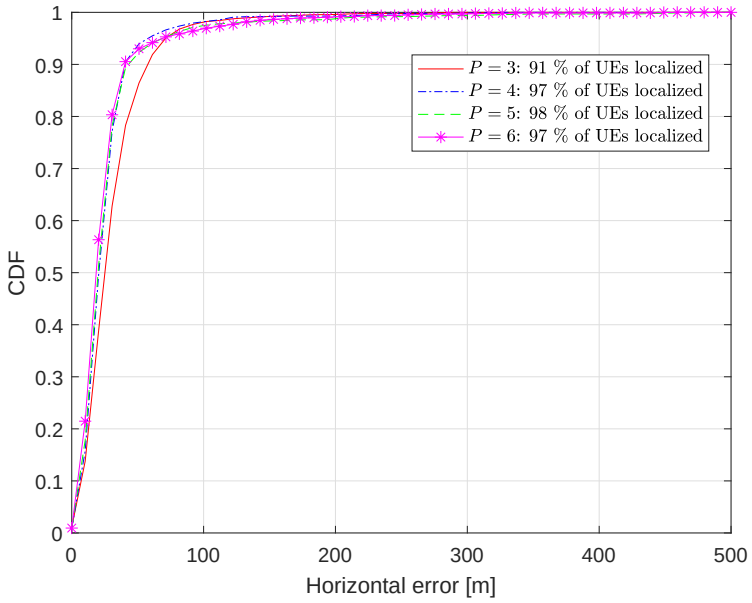

Figure 5.10: Positioning errors and localization ratios for different number of participating eNodeBs P in AWGN channel, using the proposed algorithm with SIC, FOC and interpolation.

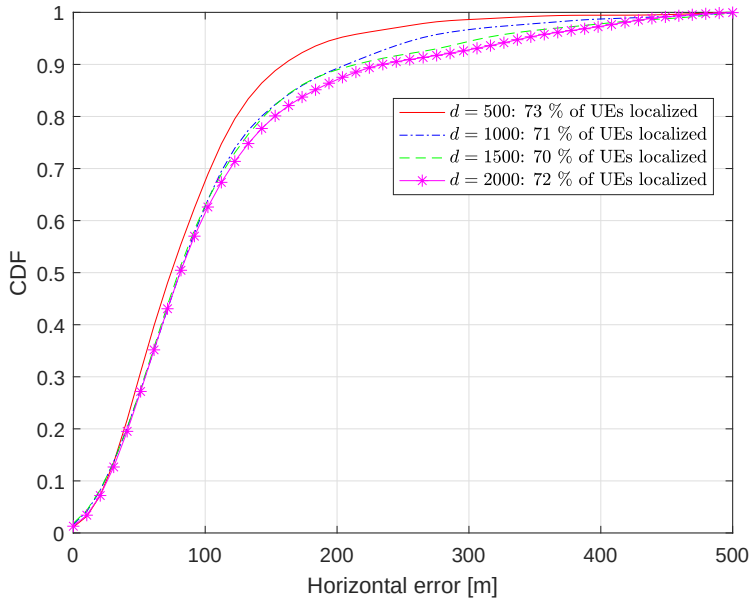

Figure 5.11: Positioning errors and localization ratios for different inter-site distances d (in meters) in AWGN channel using the standard TOA estimate.

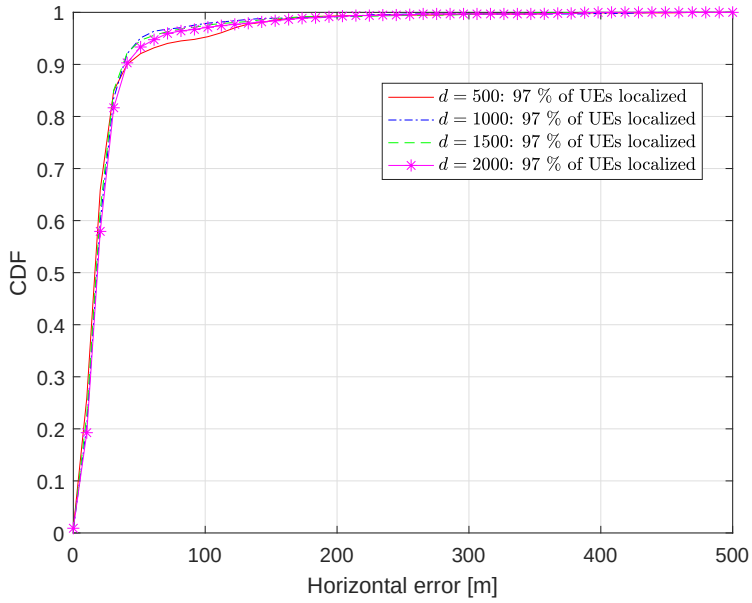

Figure 5.12: Positioning errors and localization ratios for different inter-site distances d (in meters) in AWGN channel using the proposed algorithm with SIC, FOC and interpolation.

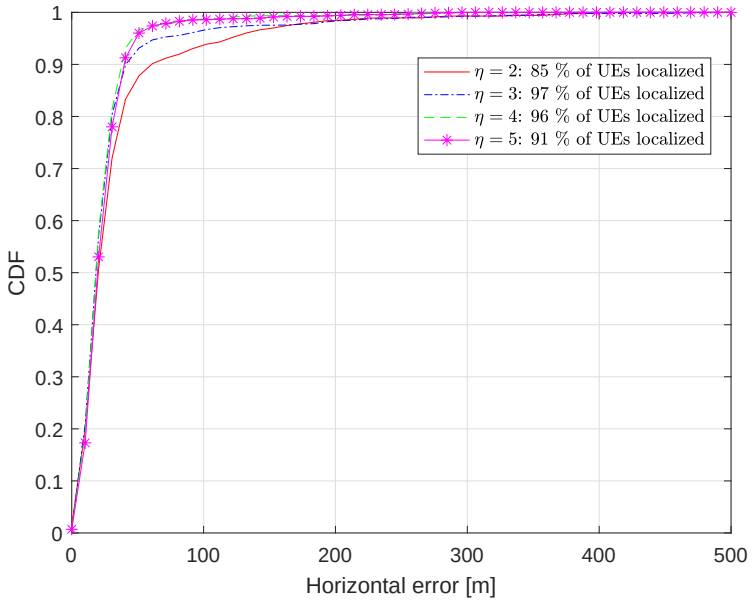

Figure 5.13: Positioning errors and localization ratios in AWGN using the proposed algorithm with SIC, FOC and interpolation with different PAR thresholds η.

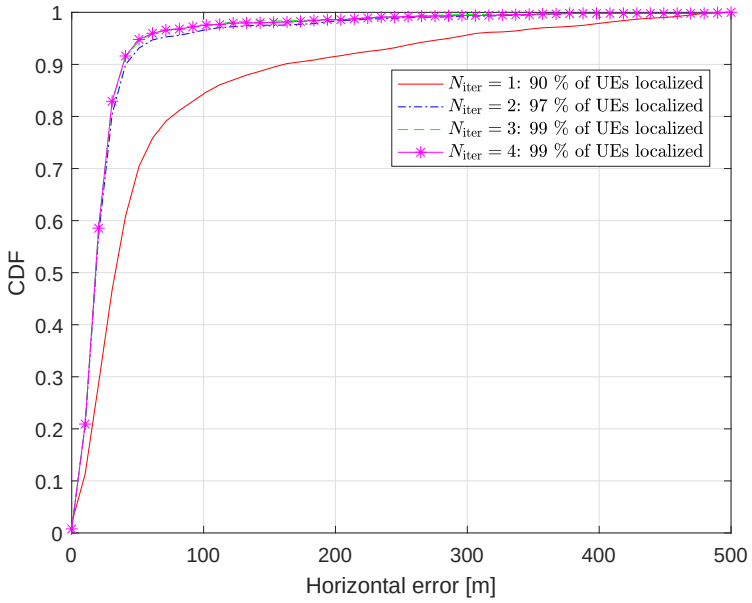

Figure 5.14: Positioning errors and localization ratios using the proposed algorithm with SIC, FOC and interpolation for different number of SIC iterations N_{iter}. As can be seen, the algorithm converges within 2-3 iterations.

5.5 Two-path Channel Simulations

Since the first-path/multipath detection block did not improve performance in the ETU channel, a simulation of TOA and positioning errors was carried out in a customized two-path channel with path delays 0 and 10 μs and corresponding average path gains of 0 and -3 dB. The results are shown in Figure 5.15 and 5.16, where it can be seen that the MPD leads to a significant performance gain in the case that the multiple path components are far away from each other, such that the peaks of each path component can be detected correctly without interfering each other, which however, is not the case for ETU channel. Therefore, a somewhat more advanced algorithm is needed to cope with the ETU channel for the first path detection, which is left as future work.

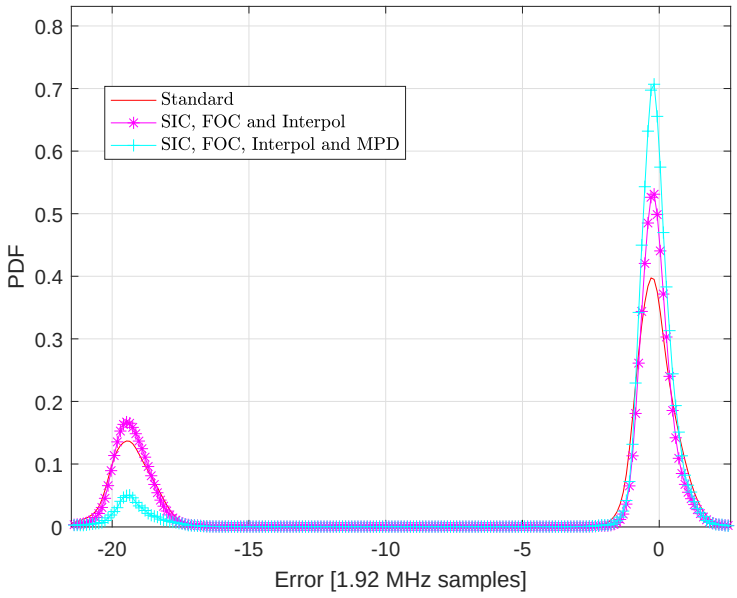

Figure 5.15: Empirical PDF of the TOA errors in the tested two-path channel.

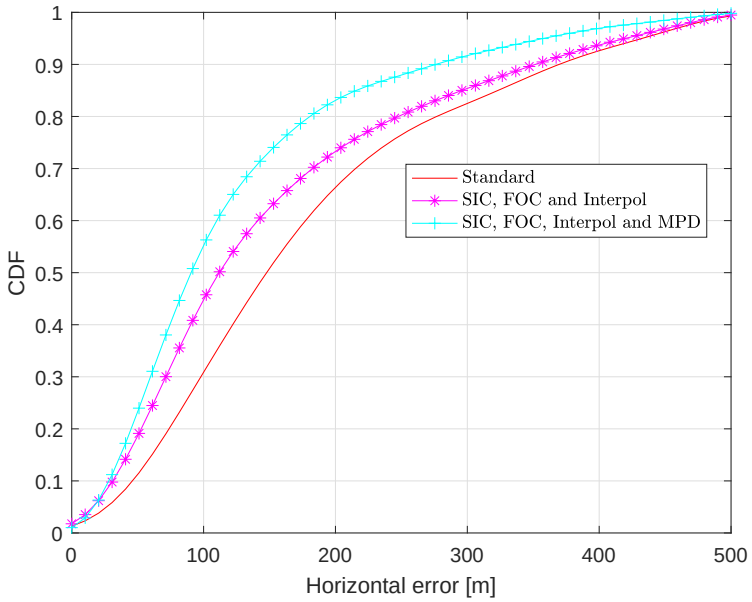

Figure 5.16: Empirical CDF of the horizontal positioning errors in the tested two-path channel.

5.6 CRLB for TOA Estimation

The TOA variance was simulated for different SNRs and compared to the CRLB. In this simulation, the number of cells was reduced to 3 and the CFO drawn between ± 750 Hz to highlight the gain of the FOC. The transmit powers were set to unity and the path loss was ignored, i.e. $G_0 = \alpha_0 = 1$, so that the SNR could be could be calculated at the receiver for each NPRS signal. The results are shown in Figure 5.17, where it can bee seen that the proposed algorithm with all three blocks almost attains the CRLB for intermediate SNRs. For high SNRs the standard deviation becomes saturated, which is due to the limited interpolation factor.

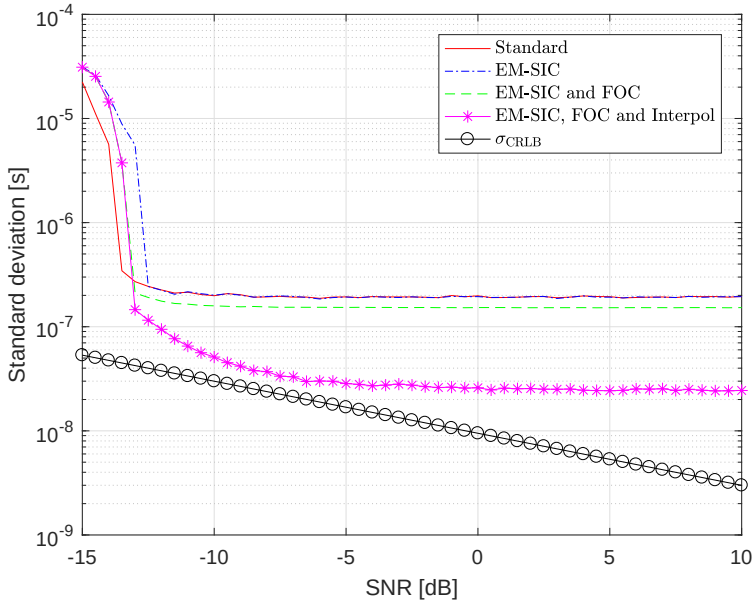

Figure 5.17: Standard deviation of the TOA estimates in AWGN compared to the CRLB for different SNR.

Chapter 6
Conclusions

From the numerical simulations, it can be seen that the proposed algorithm increases positioning performance under all circumstances. From Figure 5.2 and 5.3, it is clear that probability of correctly identifying the TOA of a received NPRS signal is doubled in AWGN and nearly doubled in ETU. Here both the SIC and FOC blocks makes a significant difference, especially in low-noise scenarios. The improvements in the probability of detection is also crucial, since determining the UE position requires the detection of at least three cells.

The TOA errors in Figure 5.4 shows that among the detected TOAs, the interpolation makes the biggest difference in terms of variance reduction. The figure also shows that the estimates are slightly biased, but this does not affect the positioning results, since the bias will cancel when the differences between TOAs are formed. Figure 5.5 shows that the benefits of interpolation are not as great in ETU channel, which is expected, since the delay between different multipath components are smaller than the sampling frequency. Therefore, the correlation peak that is being interpolated is in fact a non-coherent addition of several peaks, shifted by a sub-sample delay. In general, the low sampling frequency makes it very difficult to mitigate multipath interference, and this is the main reason for the poor TOA error performance of the proposed algorithm. The purpose of the first-path estimation block is to solve this problem, but due to the low sampling rate, it cannot distinguish the different paths for ETU. This is an issue that needs to be addressed in future work in order to improve performance in urban fading channels. However, the first-path detection is not useless, since it can decrease the TOA error variance in multipath channels with path delays significantly longer than the sampling period, such as in Figure 5.15. This shows that when the two-paths can be resolved after interpolation, the first-path detection works properly.

The AWGN positioning errors in Figure 5.6 and Table 5.2 highlights the large performance increase that the proposed algorithm yields. The 95th percentile of the position errors are decreased from 342 m to 61 m and the percentage of localized UEs is increased from 67 % to 97 %. This shows that without the presence of multipath fading, the SIC, FOC and interpolation stages all yield a significant performance increase. While the interpolation decreases the error of localized UEs, the SIC and FOC also increase the localization percentage significantly. This is illustrated in figure 5.8a, where the distribution of estimated UE positions is shown. Using the standard method, almost none of the UEs close to the cell tower in the left corner of the hexagon are localized. This is expected, since the near-far

problem is most severe when a UE is very close to a cell tower. However, when using the proposed algorithm, this problem is mitigated by interference cancellation, such that the weaker cell towers can be detected and the UEs can be localized, which is clearly seen in Figure 5.8b.

In ETU, the increase in positioning accuracy is not nearly as large, which is seen in Figure 5.7, for reasons that have already been mentioned. Nevertheless, from Table 5.3 we see that the percentage of localized UEs is increased just as much as in AWGN and that this gain primarily comes from SIC. This also illustrates the problem of comparing positioning errors for two methods where the sample sizes are different. For the two-path channel results in Figure 5.16, the results are similar, but the first-path detection is able to further decrease the position errors somewhat.

Figures 5.9-5.10 illustrates the very significant impact that the number of participating cells P has on localization and positioning performance and how the proposed algorithm takes care of this problem. Using the standard method, the number of participating cells is critical for the probability of being able to localize. Using only three cells, which is not an unrealistic scenario, only 18 % of UEs were localized, and this increases to 54 % when increasing to 4 cells. The proposed algorithm seems to be indifferent to this parameter, since the results are almost identical, independently of the choice of P. This is a very nice property, especially in rural scenarios where not many cells are available. Similarly, Figures 5.11-5.12 shows that the positioning errors seems to increase with the inter-site distance d for the standard method, whereas the proposed algorithm shows results that are independent of this parameter. Since NB-IoT is expected to be deployed with very large cell sizes, this is a nice property to have.

The results from Figure 5.13 shows that the performance of the proposed algorithm is not highly dependent of how the PAR-threshold η is set, but $\eta = 3$ or 4 is probably reasonable. The problem of choosing a good threshold can be described as a trade-off between sensitivity and specificity. A lower threshold will yield more false alarms, whereas a higher threshold results in more missed detections. Moreover, Figure 5.14 shows that 2-3 EM-SIC iterations is enough to maximize performance, as further iterations do not increase performance. The choice of N_{iter} should also take the computational complexity into account.

Finally, the results of the CRLB simulation in Figure 5.6 can be addressed by concluding that the proposed algorithm comes very close to achieving the lower bound, much closer than the standard method. For very low SNRs, the TOA variance becomes very large, since the NPRS signals are completely buried in noise and a longer signal would be necessary to improve the results. For intermediate SNRs, the bound is almost attained for the proposed method, and as the SNR increases, the variance is bounded by the low sampling rate and the interpolation factor. The variance for high SNRs could thus be further reduced by increasing the interpolation factor V, but since such low-noise scenarios are not realistic, this is not of much concern.

One important conclusion from the CRLB simulation is that since the proposed algorithm almost attains the CLRB, then at least in AWGN scenarios, performance cannot be increased much more than what has been done here. The performance is fundamentally limited by the small bandwidth of the NB-IoT NPRS signal and

this limit cannot be worked around by the UE. However, the bound can be lowered by transmitting several consecutive NPRS subframes and the proposed algorithm can easily be extended to consider such scenarios.

In summary, the following can be said about the proposed EM-SIC algorithm:

- In AWGN channel, the positioning performance is significantly increased, both in terms of accuracy and localizability. The impact of the near-far problem is reduced.
- In ETU channel, the gains are mainly in terms of localizability. The same can be said about other multipath fading channels with short path delays.
- The first-path detection does not give any benefits, unless the channel path delays are longer than the UE sampling period.
- The algorithm shows tolerance towards non-ideal positioning conditions, such as a small number of participating cells and large inter-site distances.

References

[1] ARM, "LPWAN Complete Solutions." URL: `https://www.arm.com/products/wireless-ip/lpwan-complete-solutions`, accessed 2017-05-15.

[2] V. Bhuvaneswari and R. Porkodi, "The Internet of Things (IoT) Applications and Communication Enabling Technology Standards: An Overview," *International Conference on Intelligent Computing Applications*, 2014.

[3] K. Rose, S. Eldridge, and L. Chapin, "The Internet of Things: An Overview," tech. rep., The Internet Society, October 2015.

[4] Ericsson White Paper, "Cellular Networks for Massive IoT," January 2016.

[5] R. Ratasuk, N. Mangalvedhe, Y. Zhang, M. Robert, and J.-P. Koskinen, "Overview of Narrowband IoT in LTE Rel-13," *IEEE Conference on Standards for Communications and Networking (CSCN)*, 2016.

[6] Y.-P. E. Wang, X. Lin, A. Adhikary, A. Grövlen, Y. Suia, Y. Blankenship, J. Bergman, and H. S. Razaghi, "A Primer on 3GPP Narrowband Internet of Things," *IEEE Communications Magazine*, March 2017.

[7] 3GPP TS 36.213, "Evolved Universal Terrestrial Radio Access (E-UTRA) and Evolved Universal Terrestrial Radio Access Network (E-UTRAN); Physical Layer Procedures," tech. rep., September 2016.

[8] A. Adhikary, X. Lin, and Y.-P. E. Wang, "Performance Evaluation of NB-IoT Coverage," *IEEE VTC Fall*, 2016.

[9] 3GPP TR 45.820, "Cellular System Support for Ultra Low Complexity and Low Throughput Internet of Things," tech. rep., November 2015.

[10] 3GPP RP-161901, "Revised work item proposal: Enhancements of NB-IoT," tech. rep., September 2016.

[11] B. P. Lathi and Z. Ding, *Modern Digital and Analog Communication Systems*. Oxford University Press, 4 ed., 2009.

[12] A. F. Molisch, *Wireless Communications*. John Wiley and Sons, 2005.

[13] E. Dahlman, S. Parkvall, and J. Sköld, *4G LTE/LTE-Advanced for Mobile Broadband*. Academic Press, 2011.

[14] I. K. Adusei, K. Kyamakya, and K. Jobmann, "Mobile Positioning Technologies in Cellular Networks: An Evaluation of their Performance Metrics," 2002.

[15] A. M. H. Khalel, "Master Thesis: Position Location Techniques in Wireless Communication Systems," 2010.

[16] Sven Fischer, Qualcomm Technologies Inc, "Observed Time Difference of Arrival (OTDOA) in 3GPP LTE," June 2014.

[17] 3GPP TS 36.355, "Evolved Universal Terrestrial Radio Access (E-UTRA) and Evolved Universal Terrestrial Radio Access Network (E-UTRAN); LTE Positioning Protocol (LPP)," tech. rep., March 2017.

[18] 3GPP TS 36.211, "Evolved Universal Terrestrial Radio Access (E-UTRA) and Evolved Universal Terrestrial Radio Access Network (E-UTRAN); Physical channels and modulation," tech. rep., March 2017.

[19] 3GPP TS 36.104, "Evolved Universal Terrestrial Radio Access (E-UTRA) and Evolved Universal Terrestrial Radio Access Network (E-UTRAN); Base Station (BS) radio transmission and reception," tech. rep., March 2017.

[20] S. M. Kay, *Fundamentals of Statistical Signal Processing: Estimation Theory.* PTR Prentice Hall, 1993.

[21] N. Sirola, "Closed-form Algorithms in Mobile Positioning: Myths and Misconceptions," *IEEE 7th Workshop on Positioning, Navigation and Communication*, 2010.

[22] 3GPP TS 36.133, "Evolved Universal Terrestrial Radio Access (E-UTRA) and Evolved Universal Terrestrial Radio Access Network (E-UTRAN); Requirements for support of radio resource management," tech. rep., March 2017.

[23] E. Staudinger and C. Gentner, "TDoA Subsample Delay Estimator with Multiple Access Interference Mitigation and Carrier Frequency Offset Compensation for OFDM based Systems," *IEEE 2011 8th Workshop on Positioning, Navigation and Communication*, 2011.

[24] M. Huang and W. Xu, "Enhanced LTE TOA/OTDOA Estimation with First Arriving Path Detection," *IEEE Wireless Communications and Networking Conference*, 2013.

[25] H. Rydén, A. A. Zaidi, S. M. Razavi, F. Gunnarsson, and I. Siomina, "Enhanced Time of Arrival Estimatoin and Quantization for Positioning in LTE Networks," *IEEE 27th International Symposium on Personal, Indoor and Mobile Radio Communications*, 2016.

[26] W. Xu, M. Huang, C. Zhu, and A. Dammann, "Maximum likelihood TOA and OTDOA estimation with first arriving path detection for 3GPP LTE system," *Transactions on Emerging Telecommunications Technologies*, 2014.

[27] M. Morelli and U. Mengali, "An Improved Frequency Offset Estimator for OFDM Applications," *IEEE Communications Letters* , March 1999.

[28] J. G. Proakis and D. G. Manolakis, *Digital Signal Processing: Principles, Algorithms, and Applicaitons*. Pearson, 4 ed., 2006.

[29] 3GPP TSG RAN WG1: R1-168310, "WF on simulation assumption for NB-IoT positioning," tech. rep., August 2016.